I&EC research
Industrial & Engineering Chemistry Research
pubs.acs.org/IECR
Article

Model Predictive Control of a Solar Power System with Microturbine and Thermochemical Energy Storage

Gang Xiao, Jiamin Yang, and Dong Ni*

Cite This: *Ind. Eng. Chem. Res.* 2022, 61, 13532−13558

Read Online

ACCESS | Metrics & More | Article Recommendations

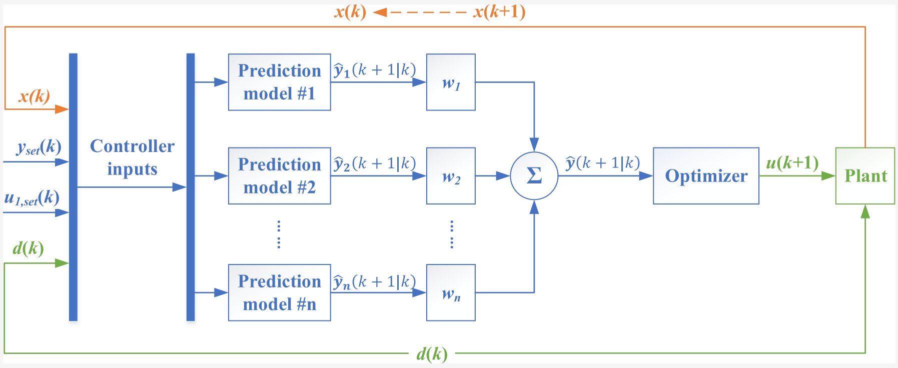

ABSTRACT: This paper presents the model predictive control (MPC) application on the solar power system with microturbine and thermochemical energy storage (TCES). To investigate the potential of a solar-powered turbine, a solar receiver and a TCES are introduced to the Brayton cycle as the replacement of the combustor. MPC is applied to offer the constrained multi-variable real-time optimization control. To increase the practicability in the solar industry, a custom-made multi-modeling approach is proposed based on the close relationship between direct normal irradiance and system states. Feedback correction mechanisms are designed to improve the prediction and target tracking accuracies. During the regulatory control under both extreme and realistic conditions, the multi-MPC (MMPC) shows stronger adaptability and reliability than proportional−integration−differentiation (PID) and higher tracking accuracies than the single-linear-model-based MPC. Although the control performance could be further improved by employing nonlinear MPC (NMPC), the much longer optimization time of NMPC was unsuitable for real-time control. MMPC is further adapted to track the grid demand, which is technically unachievable by PID in the current system. While the output power precisely follows the demand, the performance parameters can still stay close to their design values, retaining a high system efficiency. Overall, the proposed MMPC enables power demand tracking operation of solar air turbine systems, and can ensure high stability and system efficiency.

1. INTRODUCTION

There is a growing trend toward large-scale applications of clean renewable energies, such as, photovoltaic, wind power generation, and so on. The unstable and intermittent nature of renewable energies imposes a great impact on the regulation capability of the power system. The solar-powered gas turbine system with thermal energy storage (TES) is a promising solution to this. The fast dynamic response characteristics of gas turbine makes it a prime candidate as a peaking unit which responds to the load demand.[1] Furthermore, compared to the conventional solar steam turbine systems, the gas turbine system is a better match to the next-generation concentrated solar power (CSP) generation technology, thanks to its higher operating temperature, lower water consumption,[2,3] and more modest capital cost.[4] Compared to the traditional fossil fuel fired gas turbine systems, on the other hand, the introduction of CSP contributes to the environmental benefits by reducing pollutant emissions and fossil fuel consumption. The integration of TES further increases the solar share by redistributing the thermal energy on the time scale. Moreover, its large thermal inertia also helps stabilizing turbine operation by mitigating the influence of climate condition changes.[5,6] Among the TES medium candidates, thermochemical energy storage (TCES), especially the metal-oxide, shows superior advantages of high energy density, high storage temperature,

Received: May 20, 2022
Revised: July 31, 2022
Accepted: August 15, 2022
Published: August 31, 2022

https://doi.org/10.1021/acs.iecr.2c01784
Ind. Eng. Chem. Res. 2022, 61, 13532−13558

and good compatibility with air.[7−9] Thus, metal-oxide-based TCES is suitable for the solar-powered gas turbine system.

The research exploration of the solar-powered gas turbine system started in the 1990s. At first, fossil fuel combustion was preserved as the supplementary power, so TES was not considered. The solar hybrid gas turbine electric power system (SOLGATE) demonstrated the first solar tower micro gas turbine (MGT) system with a 230 kW_e generation and a nearly 60% solar share,[10−12] followed by the solar-hybrid power and cogeneration plants (SOLHYCO)[13−16] and solar up-scale gas turbine system (SOLUGAS),[2,17,18] which gradually took the solar hybrid gas turbine system toward commercialization and MW-level. AORA solar accomplished the first two commercial solar hybrid gas turbine co-generation plants in Israel (2009) and Spain (2012), respectively.[19] A solar-only MGT system was constructed by the optimized microturbine solar power system project (OMSoP) with the operation and control strategies proposed accordingly.[20,21] As the gas turbine solarization technology developed and matured, TES is integrated in pursuit of elevated solar share and prolonged operation duration. The Commonwealth Scientific and Industrial Research Organization (CSIRO) and Mitsubishi Heavy Industries (MHI) studied the integration of solar air turbine with TES via component experiments and system simulations.[22,23] In our previous work, the solar-only MGT system is studied with the addition of TCES in the CSP MGT with TES (SolGATS) project.[9] Real-time control strategies based on proportional−integration−differentiation (PID) controllers have been proposed and implemented in thermodynamic simulations.[6] This paper is the further investigation on the real-time system control.

In terms of real-time control, TES imposes a great challenge on solar-powered system control because its transient behaviors are highly affected by solar irradiance in both short-term and long-term ways.[24] In most TES-based solar systems, flow rate control is the most popular control strategy. The execution units are either pumps[24,25] or valves,[6,26] or the combination of both.[27−36] In some cases, the classical PID controller can satisfy the control requirements.[24,26,32,37] However, with the increasing system complexity, more advanced methods were attempted in TES-based solar system control. For example, the supervisory control structure is applied to solar cooling systems with storage tanks[27,28] and a combined cycle power plant with double-tank molten-salt storage,[31] respectively. The hierarchical scheme decomposes the control tasks and allocates them to different controllers, saving computational efforts while maintaining benign control performance. Navas et al.[36] included the modeling of passing clouds in the model predictive control (MPC) implementation on a solar thermal plant with double-tank molten-salt TES. The proposed MPC improved the amount of energy storage while keeping the generated electricity power on its nominal value. López-Alvarez et al.[38] focused on the optimal operation of the start-up process of thermal solar plants with energy storage tanks. By minimizing the start-up time, power demands could be satisfied more efficiently. There is also research work focusing on the control of the TES subsystem itself. Leo et al.[34] used linear quadratic regulator with integral action of output to regulate the outlet oil temperature and the tank level of the molten-salt TES. Prieto et al.[30,33,35] compared different control strategies, namely, feed-forward PID, feed-forward advanced PID, and feed-forward adaptive-predictive control and found that the third strategy presented the best stability and setpoint tracking performance. The hierarchical control scheme is also performed in the power industry. Juuso et al.[29] adopted a PI-type linguistic equation controller with predefined adaptation models on a solar collector field and designed intelligent analyzers to achieve smart working point control. Patrón et al.[39] designed a three-layer controller for post-combustion carbon capture plants, including real-time optimization, nonlinear MPC (NMPC), and moving horizon estimation. The proposed scheme effectively improved the process economics of the plants.

Unlike the solar systems mentioned above, the studied system in this work uses gas turbine for power generation. The system control in this case faces other challenges. Compared to the steam turbine systems which is the most popular power block choice in TES-based solar thermal power plants currently, gas turbine is well-known for its rapid response and compactness. The volume and thermal inertias of the additional solar components are much larger than the gas turbine itself, plus the highly coupled cycle structure, the complexity and difficulties in system dynamic control are significantly increased. Furthermore, the thermochemical reaction adds to the system's nonlinearity. To accomplish the solar-powered system control with gas turbine and TES, the gas turbine control is also of vital importance.

Many research efforts have been made in gas turbine control. Although most of them are the single-loop, non-recuperative Brayton cycle, they can still offer reference value. Besides the PID control[40] which has been widely used in commercial gas turbines, more advanced control methods are investigated to meet the increasing requirements. MPC stands out due to its advantage of constraints handling in multi-variable system control.[41] The abilities to foresee future events and conduct online optimization make it more competent to deal with disturbances.[42] The feasibility of MPC in gas turbine control was first investigated by Vroemen et al.[43] and implemented in the real-time control experiment by Essen et al.[41,44] Based on the successively linearized models and a first-order integrating filter, the NMPC performs well in constrained reference trajectory tracking. Diwanji et al.[45] developed a Weiner−Laguerre−ANN prediction model and applied NMPC in single spool gas turbine, proving the applicability of MPC in fast-dynamics nonlinear systems. To improve the control performance, Jurado[42,46] applied the Hammerstein model to perform NMPC on microturbine and used the internal model control scheme to deal with the mismatch and disturbances. Wiese et al.[47] reduced the prediction model order, augmented the optimization problem with integral action, and proved the advantages of NMPC. Mu and Rees[48−50] conducted online linearization and incorporated generalize predictive control (GPC) to control the gas turbine engine. Some researchers focused on accelerating the calculation speed and developed the block MPC[51] and the fast-MPC.[52] Martucci et al.[53] added a terminal weight term at the objective function to shorten the prediction horizon and hence speed up the calculation. MPC was also proved superior than PID and commercial control system in heavy-duty gas turbine control with shorter settling time and less oscillations.[54,55] For combined cycle gas turbine system, fuzzy predictive supervisory control[56] and GPC[57] were also attempted.

The nonlinear system dynamics imposes great challenges on model-based controller design. However, the acquirement of a comprehensive plant model is often difficult and time-consuming.[58] Moreover, the models which are able to retain

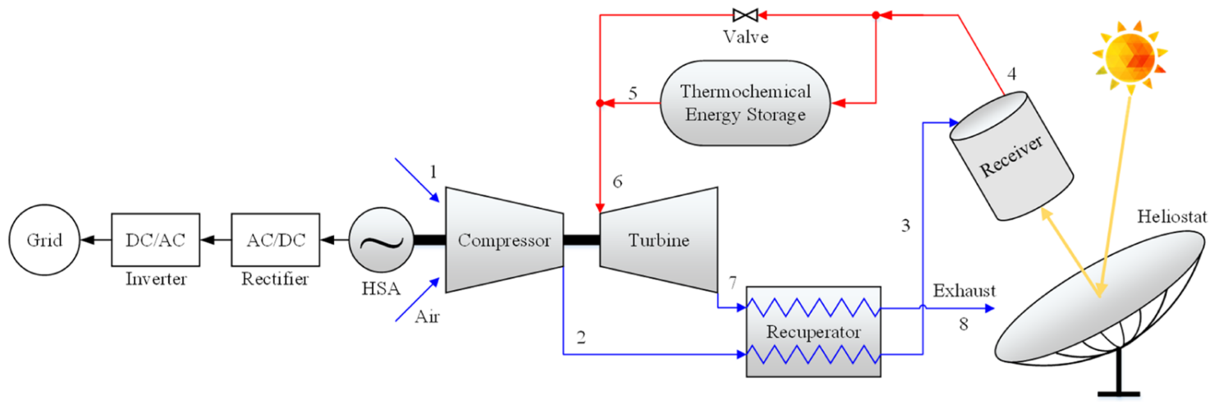

Figure 1. System scheme of the solar power system with microturbine and TCES (red: high-temperature airflow; blue: low-temperature airflow; and yellow: solar irradiance).

high prediction accuracy over wide operational ranges would require large computational efforts in receding horizon optimization, which is detrimental to real-time control.[59] Especially in large-scale application, linear or simple nonlinear prediction models usually prove stronger practicality than comprehensive nonlinear models.[60] On these basis, multi-model prediction control (MMPC) is developed. The main challenges of MMPC can be concluded in three aspects: the model division, model construction, and the model aggregation.[61] Venkat et al.[61] divided the operation regimes according to the input−output steady-state map using the fuzzy clustering technique and employed the projection technique for fuzzy aggregation. By introducing fuzziness to the clustering process, the overlaps of subspaces can smoothen the transition between local models. Schott and Bequette[62] combine the multiple local models by estimating the probabilities of each model using recursive Bayesian theorem. The resulting multi-model adaptive control presented an improved performance when moving from open-loop stable regions to open-loop unstable regions. The fuzzy modeling and recursive Bayesian probability weight were also attempted in the boiler turbine system.[63] Besides, fuzzy weight is often calculated for model aggregation in fuzzy-model-based MPCs.[64,65] Kordon et al.[66] computed multiple linear-model-based linear controllers in parallel in order to avoid unsmooth transition when switching between local models. A concurrency coordinator is used to compare all controllers' control errors and decide the next control action. As a result, stable and good closed-loop performance and bumpless transitions were obtained. More advanced algorithms are implemented to further improve the prediction precision. Wu et al.[67−69] adopted recurrent neural network and ensemble learning to improve the prediction accuracy and closed-loop performance. By using different initial weight matrices in ensemble learning, local optimum might be avoided. The ensemble regression modeling technique incorporated with MPC proved good robustness and effectiveness.

Despite these research achievements, there still exist limitations in MPC applications on TES-based solar gas turbine system control:

MPC is mostly implemented in the conventional non-recuperated Brayton cycle. The control methods are also mostly limited to the responsive fuel flow regulation. Even for the combined cycle control, the control strategies still focus on the gas turbine or TES itself, only with different controlled variables. With the promotion of gas turbine solarization, the system control is facing new challenges. The TCES-based solar air turbine system control in this work has to deal with different disturbances and manipulated variables. Thus, a new control strategy needs to be proposed.

Furthermore, the increasing cycle complexity and environmental uncertainty in the solar gas turbine system need to be comprehensively considered in system control. For example, the control strategies for short-period and long-period weather changes should be distinguished. System constraints and multi-variable control scenarios should also be considered in an optimized way. As the number of controlled variables increases, applying multiple PID control loops would massively increase the control scheme's complexity. Therefore, more advanced and reliable real-time control approaches should be adopted.

In the solar-powered gas turbine system, the influence of the fluctuating nature of solar irradiance is enhanced by the concentration technology. The thermochemical dynamics of TCES also adds to the system nonlinearity. The highly coupled cycle configuration, plus the difference between the large-inertia solar components and the fast-dynamics turbomachinery, further increases the complexity of system transient response. All these factors add to the difficulties of system control, yet they are seldom regarded in the existing publications.

Last but not least, the increasing installed capacity of unsteady renewable energies calls for their abilities to follow the load demand. Usually, the renewable energies are influenced by climate conditions and would lead to severe instability of power grid once they are connected on a large scale. Currently, the load demand tracking function is mainly handled by fuel flow regulation in the conventional gas turbine system, which is unachievable in the presented solar-only system. Moreover, it would be of vital significance if the demand tracking can be handled without the help of fossil fuel consumption.

Motivated by the concluded research gaps, this work continues the previous work on the control strategy investigation of a solar power system with microturbine and TCES[6] and implements MPC for the constrained multi-variable real-time optimization control for different applications. The operation safety, disturbance rejection, and setpoint tracking performance during wide-span off-design operation are accomplished well. The contribution of the presented work is summarized in the following aspects:

https://doi.org/10.1021/acs.iecr.2c01784
Ind. Eng. Chem. Res. 2022, 61, 13532−13558

(1) System nonlinearity is handled by a multi-modeling method, which is customized based on the close relationship between direct normal irradiance (DNI) and system states. The proposed modeling method exhibits high practicability in the CSP industry.

(2) To improve the setpoint tracking performance, feedback correction mechanisms are specially designed from three different aspects, and the prediction errors and tracking deviations are successfully reduced.

(3) With the help of MPC, the solar air turbine system is able to follow the grid power demand fast and accurately. This is unachievable by PID because the output power serves as the manipulated variable in this case. The improvement of dispatchability is of vital significance for the rapid and vast development of renewable energies.

2. SOLAR POWER SYSTEM WITH MICROTURBINE AND TCES

The solar power system with microturbine and TCES in this work is an open-loop recuperated Brayton cycle with a high-temperature solar receiver and a TCES unit. It should be noted that there is no combustor in the studied system, so that we can focus on the control strategy independent of the conventional fuel combustion. The system scheme is shown in Figure 1. The ambient air is compressed and preheated by the compressor and recuperator, respectively. Then, the pressurized and preheated air was further heated up to >800 °C in the solar receiver by the concentrated solar irradiance. The downstream TCES unit can adjust the turbine inlet temperature by absorbing the redundant energy or releasing the stored energy. Also, the large thermal inertia of TCES unit can help stabilize the air condition in the turbine inlet. Afterward, the high-temperature pressurized air expands in turbine and drives the rotor to rotate at a high speed. The high-speed alternator (HSA) connected to the compressor and turbine therefore generates electricity power which is then fed to the grid after being regulated by a rectifier and an inverter. The turbine exhaust air is then discharged to the atmosphere after heat recovery in the recuperator. The valve in parallel with TCES is a regulating valve, which decides the amount of the stored/released heat during operation. The design parameters of the major components are introduced in our previous work.[6]

In terms of system control, the rotational speed (N) of the shaft which connects the compressor, turbine, and the HSA, and the turbine outlet temperature (TOT) are supposed to be constant at their design point, in order to achieve favorable overall performance, for example, high thermal-to-electricity efficiency. Based on the system characteristics, the output electricity power and the bypass ratio of TCES unit are implemented as the manipulated variables.[6]

3. MODEL CONSTRUCTION

This section constructs the prediction model for MPC applications. For the current system, building a first-principle nonlinear model is highly complicated. Multiple nonlinear heat-transfer empirical equations have been used in heat exchanger models to consider the convective and radiative heat-transfer effects through insulations, with ambient air and within airflow channels. More importantly, some of the component models cannot obtain an analytic form. For example, the calculations of the compressor and turbine models need to look up the performance characteristic maps or tables, which adds to its difficulties to apply in MPC.

The online optimization mechanism in MPC calls for the need to lower the calculation complexity and save the computational efforts, so the linear state-space model is used to manifest the system characteristics.

3.1. System Identification for the TCES-Based Solar Air Turbine System.

To facilitate the MPC implementation, the linear state-space model is identified according to the transient operational data provided by the high-fidelity MATLAB/Simulink model, which was developed and validated in our previous work.[6] The discrete-time linear state-space model consisting of seven specific measurable states is identified according to the transient responses.

$$\begin{aligned} \boldsymbol{x}(k+1) &= \boldsymbol{A}\boldsymbol{x}(k) + \boldsymbol{B}_u\boldsymbol{u}(k) + \boldsymbol{B}_d d(k) \\ \boldsymbol{y}(k) &= \boldsymbol{C}\boldsymbol{x}(k) \end{aligned} \tag{1}$$

where $\boldsymbol{x} \in \mathbb{R}^n$, $\boldsymbol{u} \in \mathbb{R}^p$, $d \in \mathbb{R}$, and $\boldsymbol{y} \in \mathbb{R}^n$ are the states, control inputs, disturbance, and outputs. $\boldsymbol{A} \in \mathbb{R}^{n\times n}$, $\boldsymbol{B}_u \in \mathbb{R}^{n\times p}$, $\boldsymbol{B}_d \in \mathbb{R}^{n\times 1}$, and $\boldsymbol{C} \in \mathbb{R}^{n\times n}$ are the coefficient matrices derived from the identified coefficients in the multiple-input−multiple-output (MIMO) model. Specifically, the state, input, and output vectors are defined as eqs 2−5, considering the thermodynamic characteristics of each component. The state parameters cover the critical performance indicators in each component, so that the identified model can approach the thermodynamic behaviors as much as possible. The control inputs are the manipulated variables, that is, the output electrical power, PW_{out}, and the valve opening, VO, while the disturbance input is the DNI. The output variables are the control targets, that is, the TOT and the turbine rotational speed, N. The sampling times of the discrete−time state-space model and MPC are the same as that of the Simulink model, that is, 0.1 s.

$$\begin{aligned} \boldsymbol{x}(k) &= [x_1(k),\ x_2(k),\ \ldots,\ x_n(k)]^T \\ &= [P_2(k), T_{M,rcp}(k), T_{M,rcv}(k), T_{g,ave}(k), T_{s,ave}(k) \\ &\quad , TOT(k), N(k)]^T \end{aligned} \tag{2}$$

$$\begin{aligned} \boldsymbol{u}(k) &= [u_1(k),\ u_2(k),\ \ldots,\ u_p(k)]^T \\ &= [PW_{out}(k), VO(k)]^T \end{aligned} \tag{3}$$

$$d(k) = DNI(k) \tag{4}$$

$$\boldsymbol{y}(k) = [TOT(k), N(k)]^T \tag{5}$$

where P_2 is the outlet pressure of the compressor, $T_{M,rcp}$ and $T_{M,rcv}$ are the core temperature of the recuperator and receiver, respectively, $T_{g,ave}$ and $T_{s,ave}$ are the average temperature of the air and solid core in TCES, respectively, TOT is the turbine outlet temperature, and N is the turbine rotational speed.

The main goal of identification is to calculate the coefficient matrices, which describe the relationships between the present system inputs, present system states, and the next moment's system states. Since the input and state vectors have been settled, disregarding the measurement errors, the multi-variable linear regression method is adopted to obtain the MIMO state-space models. In the view of industrial applications, the

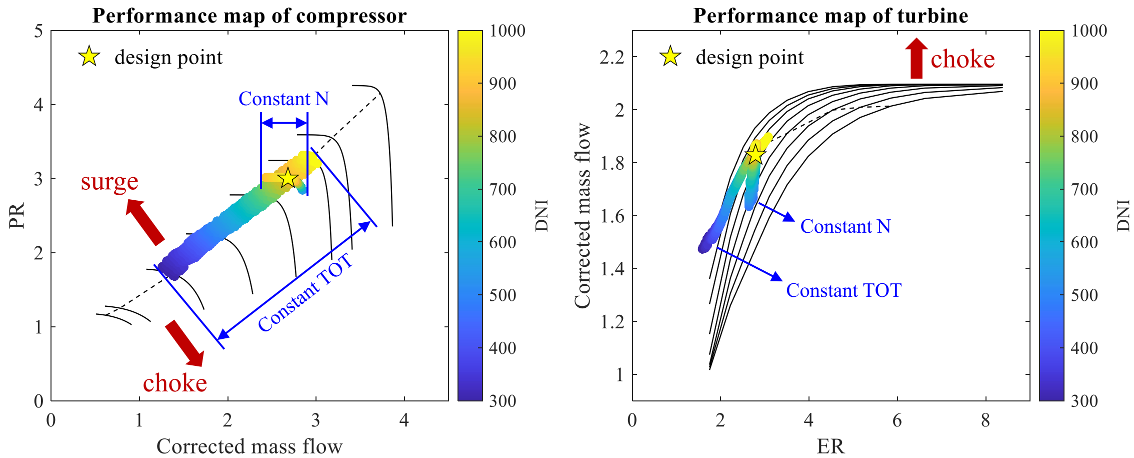

Figure 2. Performance maps under constant *N* and constant *TOT* operation strategies (each point represents a steady operational state. *PR*: pressure ratio, *ER*: expansion ratio, and *DNI*: direct normal irradiance. The surge and choke areas are beyond the areas that solid lines cover).

proposed modeling method has high practicability and is easy to implement in practice.

3.2. Multi-Modeling Method for the TCES-Based Solar Air Turbine System. Compared to nonlinear models, the linearized model may cause large prediction errors when the situation deviates far from the design condition, so a multi-modeling approach is implemented to better handle the wide-span off-design situations.

In order to decide the division of the prediction model into multiple ones, the operational steady states of the power system are analyzed with respect to different DNIs and operation strategies because DNI is one of the most important indicators in the CSP industry. The two most important performance indicators are taken as examples, that is, N and TOT. According to the previous investigation on the proposed system,[6] under varied DNI conditions, when either of them is kept constant at design point, that is, 120 krpm and 923 K, respectively, the system's optimum steady states are calculated and displayed on the performance maps of the compressor and turbine, as shown in Figure 2. These performance maps are vital analytical tools of turbomachinery components' working performance. The solid lines in display are the constant corrected speed lines. The dash lines are the maximum isentropic efficiency lines. The operation state is expected to be closer to the dash lines, where the compressor and turbine's performances are better.

Intuitively, these two operation strategies show different but complementary characteristics. The patterns of constant *N* operation are similar to the constant corrected speed lines (black solid lines) and its state changes less, while those of constant *TOT* operations adhere to the maximum isentropic efficiency line and yet vary a lot wider than constant *N* operations. The authors hope to combine the advantages of both strategies, so both *N* and *TOT*'s setpoints tracing are considered in the following sections. In the practical application, the operation region would be around these presented colorful points.

Another important conclusion is that the variations of the performances are consistent with that of *DNI*. The system states are mainly determined by the energy equilibrium between the input, storage, and output. The energy storage is restricted by its large thermal inertia and relatively small energy density compared to the CSP, while the output electrical power has better flexibility in the grid-connected scenario and serves as the manipulated variable. *DNI* is the critical influencing factor on system states. Plus, as the basic performance indicator of solar energy, it is of convenient availability in solar power plants. Thus, by partitioning the models with respect to different *DNI*s, the system states are divided in an organized way.

To further explore the relationship between *DNI* and system's state transition pattern, 25 linear state-space models are identified every 12.5 W/m^2, ranging from 550 to 850 W/m^2 (basically covering the whole operation scale of *DNI* in practice). Each model centers at a certain *DNI* and covers around ±20 W/m^2. The variation patterns of the state transition matrix, $\boldsymbol{A}$, and the input coefficient matrix, $\boldsymbol{B}$, of the 25 state-space models are investigated.

First, linear regression on each element of the matrices was conducted. Results showed that the fitting degree indicators, R^2, are higher than 0.85 for 41% and 86% elements in $\boldsymbol{A}$ and $\boldsymbol{B}$, respectively. Moreover, for every three successive models, linear interpolation was conducted with the two side models to obtain a new middle model. The distance between the two middle models is considered as an indicator of the nonlinearity between these three models. As displayed in Figure 3, with the

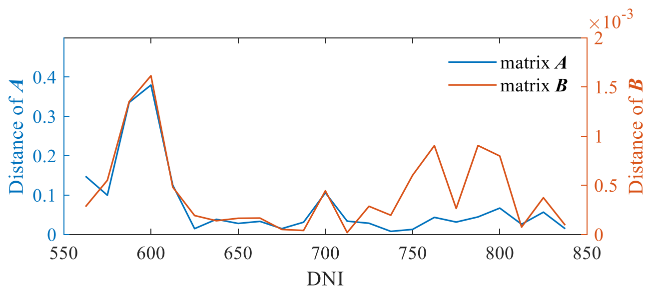

Figure 3. Distribution of the distances of matrices $\boldsymbol{A}$ and $\boldsymbol{B}$.

variation of *DNI*, the distances of both matrices $\boldsymbol{A}$ and $\boldsymbol{B}$ vary on the same scale. Thus, despite the existence of nonlinearity to some extents, the variations of state transition matrix and input coefficient matrix are basically consistent, so it should be viable to partition the models along with *DNI* in a uniform manner.

Ideally, the partition interval should be as thin as possible in pursuit of the best prediction accuracy. However, it would impose great computational burden on the processor and is

https://doi.org/10.1021/acs.iecr.2c01784
Ind. Eng. Chem. Res. 2022, 61, 13532−13558

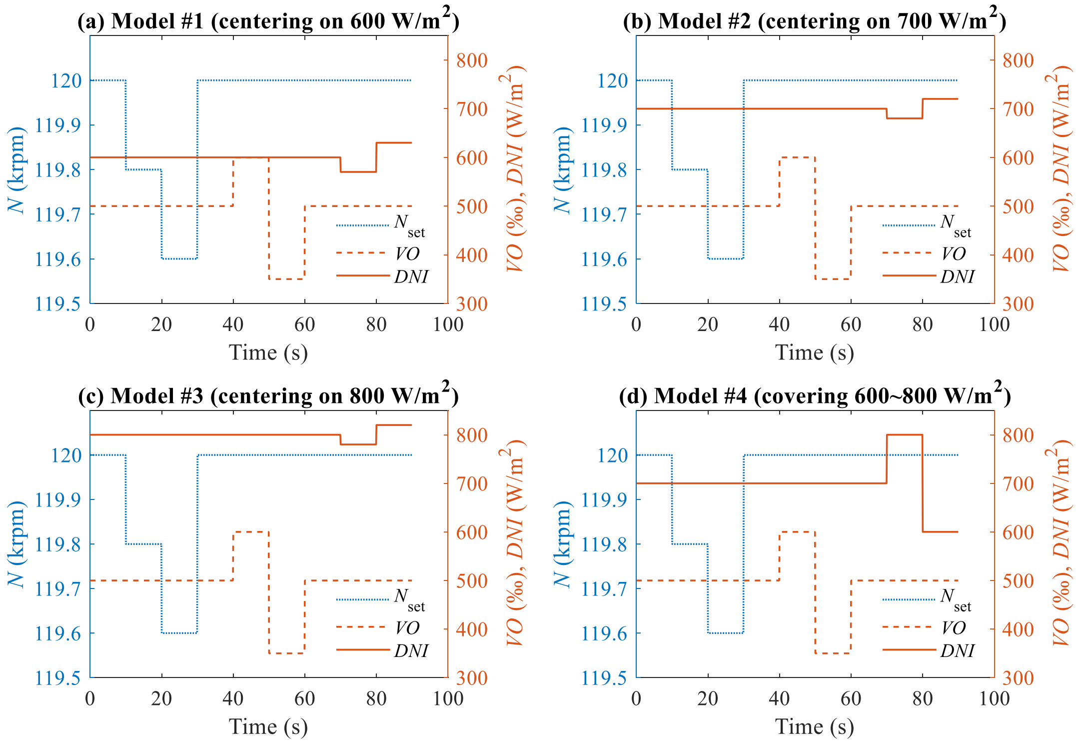

Figure 4. Input signals for model identification.

impractical in the industrial application. To demonstrate the feasibility of MMPC, three linearized models are used to predict the system dynamic response on the *DNI* scale of 550−850 W/m^2.

An optimization problem is built to decide the partitioning. The whole *DNI* scale is divided in three sections. In each section, the distances between every two models' matrices $\boldsymbol{A}$ or $\boldsymbol{B}$ are calculated, in order to characterize the similarities of the models in the same section. The sum of all distances in three sections is then minimized through optimization. The optimal partitioning plans for matrix $\boldsymbol{A}$ and $\boldsymbol{B}$ are centering 600, 712.5, 812.5 and 575, 662.5, 800 W/m^2, respectively. Therefore, regarding both optimization results, three linear models centering on 600, 700, and 800 W/m^2 are chosen for MMPC implementation in the following sections. Note that the combination of 600, 700, and 800 W/m^2 is also one of the local minima, and its objective function's value is very close to the global optimum results.

Overall, the abovementioned system identification and multi-modeling methods are proposed by taking advantage of the close relationship between *DNI* and system state. They can provide high practicability and reliability in the CSP industry application.

Remark 1

The majority of the current work has been conducted in simulations which, however, cannot completely reflect the characteristic of the real situations. There is an inevitable disparity between the nonlinear model we derived and the real-world condition. Thus, to obtain a fair result, it is more valuable to perform the comparison between NMPC and MMPC, according to real objects and real dynamic processes. Alternatively, there is another potential way to approximate the realistic condition, that is, to consider uncertainty in prediction model parameters.[70,71] When system parameters are uncertain and with probability distributions, the closed-loop nonlinear behaviors can be treated as a linear model with uncertainties. Although the control performance superiority over using the nonlinear model is not guaranteed, the process nonlinearities resulted from the disturbances are included. By using this robust modeling method, the process variability and feasibility can be evaluated, and the asymptotic stability can also be strictly enforced. However, the presented work focuses on the multi-modeling approach, so this will not be discussed in further detail.

3.3. Linear Model Validation. In this section, three prediction models are identified near the design point (DNI = 800 W/m^2) via multi-variable linear regression, centering on 600, 700, and 800 W/m^2, respectively, with ≤50 W/m^2 variation. For comparison, another linear prediction model covering 600−800 W/m^2 is also identified for MPC.

To generate the transient response data, the Simulink model starts with a specific *DNI*, which is the central value of the operating *DNI* range. The *DNI* is kept constant until the system reaches steady state. After this, the data collection for model identification begins, and multiple step changes of system inputs are imposed. Given the fact that without any control actions, the solar air turbine system would be highly unstable, the transient data for identification are therefore obtained in the constant speed mode with power regulation.[6] The input signals after the beginning of data collection are displayed in Figure 4. Each diagram displays one model's input signals. The sampling time is 0.1 s. The value of the step-change frequency is chosen based on the different response rates of the physical parameters. The time constants of the temperatures are at minute-to-hour scale, while those of the pressure and rotational speed are at millisecond-to-second scale. The step-change frequency is finally determined through multiple tests, which aim at improving the prediction accuracies of the identified models.

https://doi.org/10.1021/acs.iecr.2c01784
Ind. Eng. Chem. Res. 2022, 61, 13532−13558

Table 1. Regression and Dynamic Simulation Errors of the Linear Model Identification[a]

Prediction model	P_2 kPa	$T_{M,rcp}$ K	$T_{M,rcv}$ K	$T_{g,ave}$ K	$T_{s,ave}$ K	TOT K	N krpm
	Regression error						
#1 (centering on 600 W/m^2)	0.010	0.000	0.000	0.005	0.000	0.121	0.000
#2 (centering on 700 W/m^2)	0.012	0.000	0.000	0.006	0.000	0.176	0.000
#3 (centering on 800 W/m^2)	0.016	0.000	0.000	0.008	0.000	0.241	0.000
#4 (covering 600~800 W/m^2)	**0.015**	**0.000**	**0.000**	**0.007**	**0.000**	**0.160**	**0.000**
	Dynamic simulation error						
#1 (centering on 600 W/m^2)	0.421	0.008	0.022	0.018	0.002	0.290	0.094
#2 (centering on 700 W/m^2)	0.394	0.011	0.016	0.025	0.003	0.309	0.084
#3 (centering on 800 W/m^2)	0.088	0.010	0.002	0.023	0.003	0.181	0.013
#4 (covering 600~800 W/m^2)	**0.564**	**0.014**	**0.023**	**0.026**	**0.002**	**0.386**	**0.124**

[a]The data are displayed with three significant figures.

The regression and dynamic simulation errors of these identified models are summarized in Table 1. Regression error is the assessment of the fitting performance of linear regression. Dynamic simulation error represents the fitting performance between the identification data and the dynamic state response data generated by the identified state-space model using the same input sequence. Note that the dynamic simulation results, although obtained with the same input sequence, are influenced by the error accumulation from each time step, therefore proving the model's practicability in dynamic applications. The simulation duration of each dynamic simulation is 90 s (900 sampling times), which is much longer than the prediction horizon in the following work, that is, 1 s (10 sampling times).

As shown in Table 1, the regression errors are generally low. Some of the errors are below 0.001 K or 0.001 krpm, so they are not displayed due to the significant figures. In terms of the dynamic simulation errors, model #4's errors are mostly larger than the others because of its wider *DNI* span in its identification data. Such a difference is more pronounced in P_2, TOT, and N, resulting from the faster dynamics in turbomachinery components. This also indicates the bigger challenge in turbine control.

Nonetheless, the overall dynamic simulation errors are at a low level, plus the long simulation or to say error accumulation time, it can be safely concluded that the linearized models obtained from the proposed model construction method are able to represent the nonlinear TCES-based solar air turbine system with high prediction accuracy and physical interpretability.

4. REGULATORY CONTROL

In this section, in order to ensure system stability in off-design operations and state transitions, an MMPC controller is designed for regulatory control, including multiple setpoints tracking and steady design point operation under actual weather conditions. The controllers' performances are discussed in comparison with three different controllers, namely, the PID control from our previous work, the single-model-based MPC, and a first-principle-model-based NMPC. In pursuit of fair performance comparison, feedback correction is also applied to MPC and NMPC. There is no feedback correction in PID due to the absence of model prediction in PID and its ability to eliminate control deviation via integration.

4.1. MMPC for Regulatory Control. Figure 5 shows the proposed MMPC scheme for regulatory control. It is built on the basis of several prediction models. During MMPC operation, all the prediction models function simultaneously based on the real-time measured states $\boldsymbol{x}(k)$ and disturbance $d(k)$. The measured states are used as the initial states of the prediction models as a part of the feedback correction mechanism. Under normal circumstances, the disturbance, that is, *DNI*, is monitored in real time in each solar power plant. If accidental equipment failure occurs and measured *DNI* is unavailable, the $d(k)$ can be treated equal to the last monitored value or the average DNI value derived from the historical data. The predicted outputs $\hat{y}$ of each model are then weighted into one to offer a comprehensive model output prediction, based on which the optimizer calculates the optimal control instructions. The optimization problem, as explained in eq 6, is to minimize the deviations of N and TOT from their

https://doi.org/10.1021/acs.iecr.2c01784
Ind. Eng. Chem. Res. 2022, 61, 13532−13558

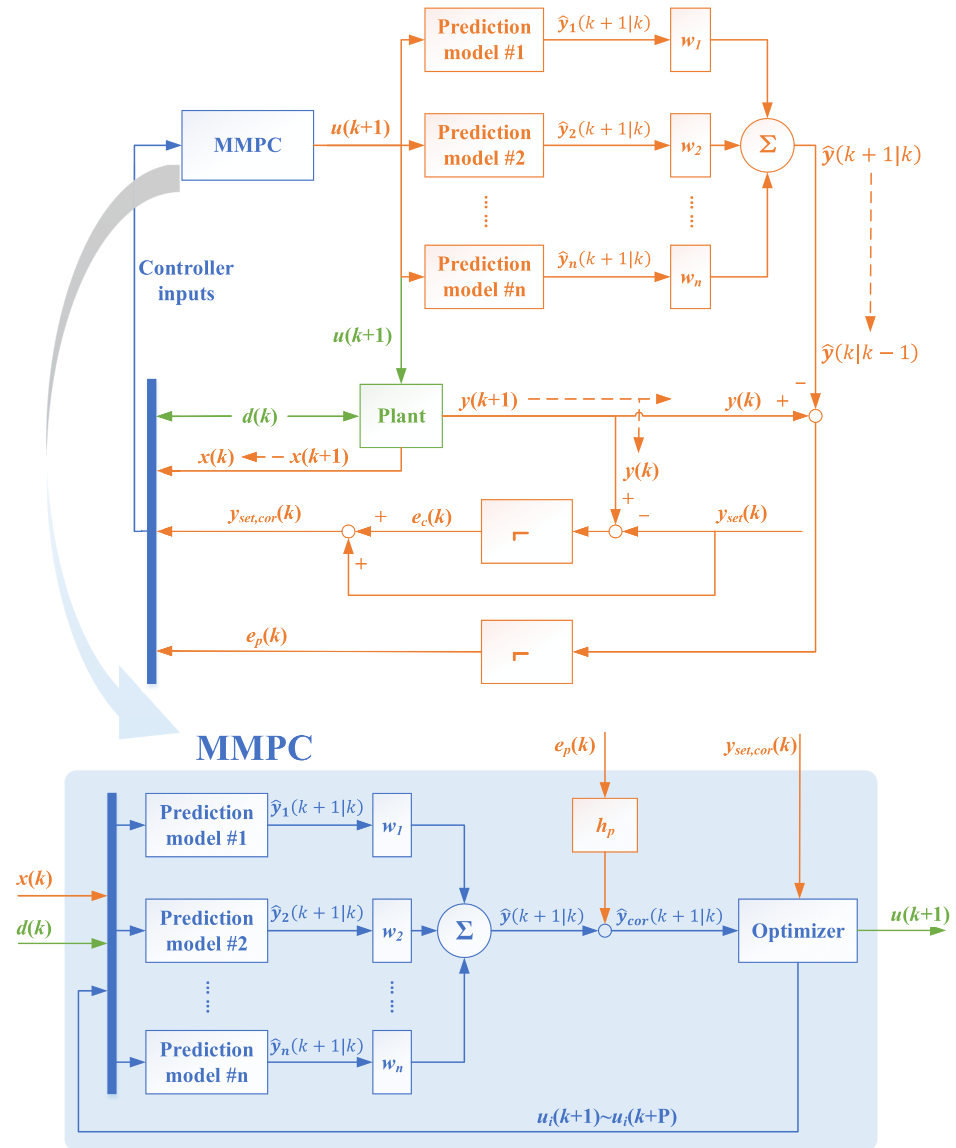

Figure 5. Schematic of MMPC for regulatory control (blue: prediction model and optimizer; green: plant model; and orange: feedback correction. The dash line indicates the state transition between the adjacent time steps. The single MPC mechanism is further explained in the extension block).

desired values and the increments of manipulated variables, that is, PW_{out} and VO.

$$
\begin{aligned}
&\min J(k) = \left\| \boldsymbol{y}_{\text{set,cor}}(k) - \hat{\boldsymbol{y}}_{\text{cor}}(k) \right\|_{\boldsymbol{Q}}^{2} + \|\Delta \boldsymbol{u}(k)\|_{\boldsymbol{R}}^{2} \\
&\text{s. t. } \boldsymbol{x}(k+1) = \boldsymbol{A}\boldsymbol{x}(k) + \boldsymbol{B}_u\boldsymbol{u}(k) + \boldsymbol{B}_d d(k) \\
&\quad \boldsymbol{y}(k) = \boldsymbol{C}\boldsymbol{x}(k) \\
&\boldsymbol{u}_{\min} \le \boldsymbol{u}(k) \le \boldsymbol{u}_{\max}
\end{aligned} \tag{6}
$$

where $\boldsymbol{y}_{\text{set,cor}}$ and $\hat{\boldsymbol{y}}_{\text{cor}}$ are the setpoint and the predicted outputs after feedback correction, respectively, $\Delta\boldsymbol{u}$ is the increments of system inputs, k is the current sampling step, $\boldsymbol{Q}$ and $\boldsymbol{R}$ are the penalty coefficient matrices, $\boldsymbol{Q} = diag(\mathrm{Q}_{\mathrm{TOT}}, \mathrm{Q}_{\mathrm{N}})$, $\mathrm{Q}_{\mathrm{TOT}} = diag[q_{\mathrm{TOT}}(1), ..., q_{\mathrm{TOT}}(P)]$, $\mathrm{Q}_{\mathrm{N}} = diag[q_{\mathrm{N}}(1), ..., q_{\mathrm{N}}(P)]$, $\boldsymbol{R} = diag(\boldsymbol{R}_{\mathrm{PWout}}, R_{\mathrm{VO}})$, $\boldsymbol{R}_{\mathrm{PWout}} = diag[r_{\mathrm{PWout}}(1), ..., r_{\mathrm{PWout}}(M)]$, $\boldsymbol{R}_{\mathrm{VO}} = diag[r_{\mathrm{VO}}(1), ..., r_{\mathrm{VO}}(M)]$, and q and r are the penalty coefficients. If setpoint tracking has the priority, then the value of q should be increased. If smooth operation of manipulated variables is more important, then the value of r should be increased. By regulating the relative value of different qs, the control preference of N and TOT can be adjusted, respectively. The same goes for the rs with PW_{out} and VO. P and M are the prediction horizon and control horizon, respectively. They are set as 1 s (10 sampling times) and 0.2 s (2 sampling times), respectively, regarding both control performance and computational efforts. The physical limitations of the manipulated variables are also considered in the optimizers as hard constraints.

Thereafter, the final adopted control instruction $\boldsymbol{u}(k+1)$ would act on the plant model in the next sampling period. Before that, $\boldsymbol{u}(k+1)$ also acts on all the prediction models to obtain new predicted outputs, the weighted results of which are consequently used to calculate the prediction errors, $\boldsymbol{e}_p$, for feedback correction on the predicted outputs. As explained in eqs 7–9, the one-step prediction errors are accumulated since the simulation starts and compensate for the latest predicted outputs.

https://doi.org/10.1021/acs.iecr.2c01784
Ind. Eng. Chem. Res. 2022, 61, 13532−13558

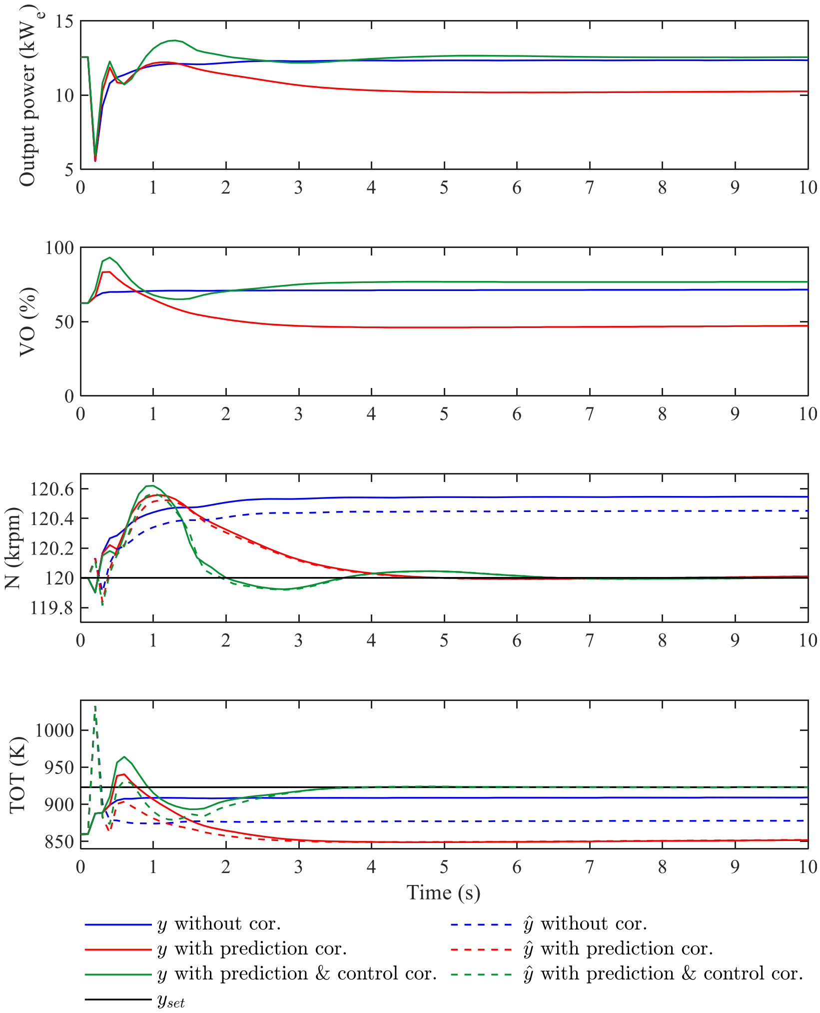

Figure 6. MMPC performances with and without feedback corrections (blue: without prediction nor control corrections; red: with prediction correction; green: with prediction and control corrections; solid line: system inputs and outputs, setpoints; and dash line: predicted outputs).

$$\hat{\boldsymbol{y}}_{\mathbf{cor}}(k) = \hat{\boldsymbol{y}}(k) + \boldsymbol{h}_p \cdot \boldsymbol{e}_p(k) = \hat{\boldsymbol{y}}(k) + \boldsymbol{h}_p \cdot \sum_{j=1}^{k-1} [\boldsymbol{y}(j) - \hat{\boldsymbol{y}}(j)] \tag{7}$$

$$\hat{\boldsymbol{y}}_{\mathbf{cor}}(k) = \begin{bmatrix} TO\hat{}T_{\mathrm{cor}}(k+1|k),\ \hat{N}_{\mathrm{cor}}(k+1|k) \\ \vdots \\ TO\hat{}T_{\mathrm{cor}}(k+P|k),\ \hat{N}_{\mathrm{cor}}(k+P|k) \end{bmatrix} \tag{8}$$

$$\hat{\boldsymbol{y}}(k) = \begin{bmatrix} T\hat{O}T(k+1|k),\ \hat{N}(k+1|k) \\ \vdots \\ T\hat{O}T(k+P|k),\ \hat{N}(k+P|k) \end{bmatrix} \tag{9}$$

where $\hat{\boldsymbol{y}}$ is the predicted outputs, $\boldsymbol{h}_\mathbf{p}$ is the correction coefficient, and $\boldsymbol{e}_\mathbf{p}$ is the accumulated historical prediction errors.

Another feedback correction mechanism is designed to eliminate the control deviations. The setpoint values for the open-loop optimization are regulated by the accumulation of the tracking errors. As introduced in 10, the deviations of system outputs from their setpoints are accumulated and serve as a compensation offset of the setpoints.

$$\begin{aligned} \boldsymbol{y}_{\mathbf{set,cor}}(k) &= \boldsymbol{y}_{\mathbf{set}}(k) + \boldsymbol{h}_\mathbf{c} \cdot \boldsymbol{e}_\mathbf{c}(k) \\ &= \boldsymbol{y}_{\mathbf{set}}(k) + \boldsymbol{h}_\mathbf{c} \cdot \sum_{j=1}^{k-1} [\boldsymbol{y}(j) - \boldsymbol{y}_{\boldsymbol{set}}(j)] \end{aligned} \tag{10}$$

$$\boldsymbol{y}_{\mathbf{set,cor}}(k) = \begin{bmatrix} TOT_{\mathrm{set,cor}}(k+1),\ N_{\mathrm{set,cor}}(k+1) \\ \vdots \\ TOT_{\mathrm{set,cor}}(k+P),\ N_{\mathrm{set,cor}}(k+P) \end{bmatrix} \tag{11}$$

$$\boldsymbol{y}_{\mathbf{set}}(k) = \begin{bmatrix} TOT_{\mathrm{set}}(k+1),\ N_{\mathrm{set}}(k+1) \\ \vdots \\ TOT_{\mathrm{set}}(k+P),\ N_{\mathrm{set}}(k+P) \end{bmatrix} \tag{12}$$

where $\boldsymbol{y}_{\mathbf{set}}$ is the setpoints of system outputs, $\boldsymbol{h}_\mathbf{c}$ is the correction coefficient, and $\boldsymbol{e}_\mathbf{c}$ is the accumulated historical control deviations.

The weighting mechanisms in optimizer and feedback correction are the same, and they are designed according to the *DNI* conditions. As explained in eq 13, the closer $DNI(k)$ approaches to DNI_i, the larger the weight is. The newly predicted outputs ensures that the model predictions are conducted with the same inputs of the plant system, thus

https://doi.org/10.1021/acs.iecr.2c01784
Ind. Eng. Chem. Res. 2022, 61, 13532−13558

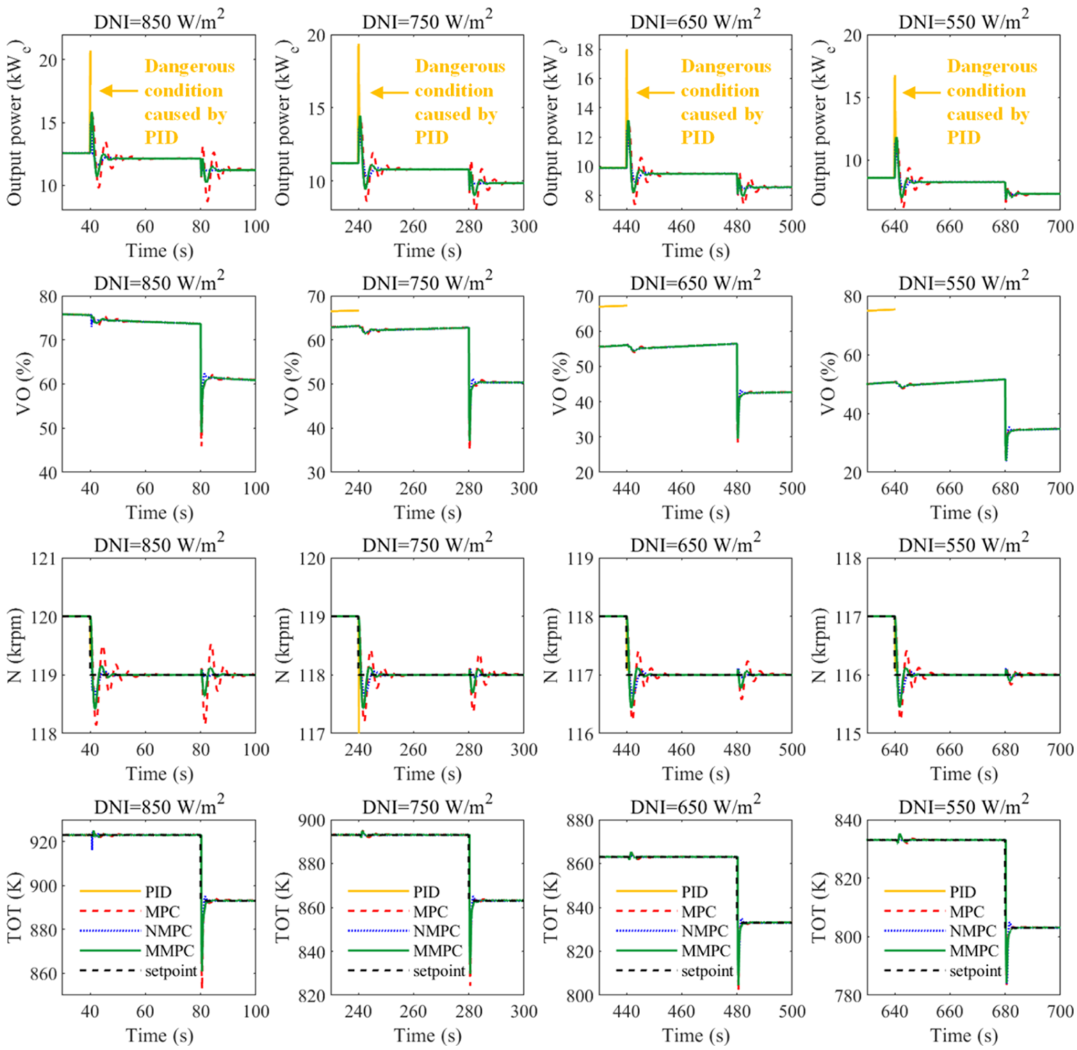

Figure 7. Transient response of step-change setpoint tracking (each column represents different *DNI* conditions. Each row displays different variables. Yellow solid line: PID; red dash line: MPC; blue dotted line: NMPC; green solid line: MMPC; and black dash line: setpoint).

improving the prediction correction performance. Due to the fact that *DNI* is unpredictable in the current work and the prediction horizon is set as 1 s, it should be safe to consider *DNI* constant within the prediction horizon and so is the computed weight.

$$w_i(k) = \frac{1 - \frac{|DNI(k) - DNI_i|}{DNI_i}}{\sum_{i=1}^{n}\left[1 - \frac{|DNI(k) - DNI_i|}{DNI_i}\right]} \tag{13}$$

where DNI_i is the center *DNI* value during model identification and n is the total number of prediction models.

The open-loop finite-horizon optimization is conducted afterward using the sequential quadratic programming algorithm in MATLAB toolbox. Only the first element of the optimal input vector, that is, $\boldsymbol{u}(k+1)$, is then applied to the mathematical model for the next sampling period. The same procedure is repeated in the next time step with updated initial states for the prediction models, thus forming the receding horizon optimization mechanism in MMPC.

Figure 6 compares the closed-loop MMPC performances with different degrees of feedback corrections. The setpoints of N and TOT are 120 krpm and 923 K, respectively, and the system starts at a steady state of 120 krpm and 860 K. *DNI* stays at 800 W/m^2 during the whole simulation. The prediction correction coefficients, $\boldsymbol{h}_p$, for N and TOT are 0.1 and 0.13, respectively. The control correction coefficients, $\boldsymbol{h}_c$, for N and TOT are −0.1 and −0.1, respectively. The penalty coefficients q for N and TOT are 80 and 10, respectively. The penalty coefficients r for PW_{out} and VO are 5 and 0.5, respectively.

In the absence of both the prediction and control corrections (blue), there exist some small yet improvable control deviations in the resultant N and TOT, that is, 0.55 krpm (0.5%) and 14 K (1.5%), respectively, with prediction errors of 0.1 krpm (0.08%) and 31 K (3.4%), respectively. By introducing the prediction correction mechanism (red), the prediction errors are reduced to <0.001 krpm (0.001%) and <0.3 K (0.03%), respectively. The N control deviation also decreases to <0.01 krpm (0.01%). However, the TOT control deviation increases to 71 K (7.7%), proving the limitations in prediction correction. Only the one-step prediction errors participate in the feedback correction, while the errors in the rest of the prediction horizon show different patterns which cannot be entirely compensated. To address this problem, control correction is implemented (green), and the prediction errors and control deviations of N and TOT are all reduced to <0.01% consequently.

https://doi.org/10.1021/acs.iecr.2c01784
Ind. Eng. Chem. Res. 2022, 61, 13532−13558

Table 2. Control Performance of Setpoint Tracking[a]

DNI	Method	$RMSE_N$ (krpm)	$RMSE_{TOT}$ (K)	$E\left(\frac{dPW_{out}}{dt}\right)$ (kW_e/s)	$E\left(\frac{dVO}{dt}\right)$ (%/s)	OS_N (krpm)	OS_{TOT} (K)
850 W/m^2	MPC	0.212	3.607	0.501	0.861	0.856	40.117
	NMPC	0.092	2.494	0.133	0.569	0.336	19.140
	MMPC	0.122	3.020	0.255	0.693	0.585	32.145
	MMPC VS MPC	**0.090**	**0.587**	**0.246**	**0.169**	**0.271**	**7.972**
	MMPC VS NMPC	**-0.030**	**-0.526**	**-0.122**	**-0.124**	**-0.249**	**-13.005**
750 W/m^2	MPC	0.180	3.417	0.414	0.813	0.799	38.729
	NMPC	0.099	2.478	0.130	0.459	0.382	19.454
	MMPC	0.119	3.011	0.239	0.731	0.571	32.951
	MMPC VS MPC	**0.061**	**0.406**	**0.175**	**0.081**	**0.228**	**5.778**
	MMPC VS NMPC	**-0.020**	**-0.533**	**-0.109**	**-0.273**	**-0.189**	**-13.497**
650 W/m^2	MPC	0.161	2.985	0.356	0.739	0.775	31.094
	NMPC	0.097	2.473	0.135	0.528	0.365	18.992
	MMPC	0.114	2.802	0.219	0.677	0.560	28.419
	MMPC VS MPC	**0.046**	**0.182**	**0.137**	**0.061**	**0.214**	**2.675**
	MMPC VS NMPC	**-0.017**	**-0.329**	**-0.084**	**-0.149**	**-0.195**	**-9.427**
550 W/m^2	MPC	0.149	2.430	0.301	0.683	0.766	19.516
	NMPC	0.096	2.464	0.138	0.652	0.352	19.066
	MMPC	0.110	2.387	0.195	0.654	0.552	18.607
	MMPC VS MPC	**0.039**	**0.044**	**0.106**	**0.029**	**0.215**	**0.908**
	MMPC VS NMPC	**-0.014**	**0.077**	**-0.057**	**-0.002**	**-0.200**	**0.459**
Average	MPC	0.175	3.110	0.393	0.774	0.799	32.364
	NMPC	0.096	2.477	0.134	0.552	0.359	19.163
	MMPC	0.116	2.805	0.227	0.689	0.567	28.031
	MMPC VS MPC	**0.059**	**0.305**	**0.166**	**0.085**	**0.232**	**4.333**
	MMPC VS NMPC	**-0.020**	**-0.328**	**-0.093**	**-0.137**	**-0.208**	**-8.868**

[a]The data are displayed with three significant figures. *RMSE* is the root-mean-square error, *E* is the mathematical expectation, and *OS* is the overshoot. MMPC's improvements = MPC/NMPC's value − MMPC's value. Green: positive improvements and red: degressions.

4.2. Case Study. In this section, the MMPC regulatory control performances under different application scenarios are studied in comparison with PID, MPC, and NMPC control. The step-change setpoint tracking is first conducted to evaluate the controllers' reliability under extreme conditions. Then, the controllers are tested in design point operation under actual *DNI* variation to prove their practicability of long-running operation in representative realistic conditions. The PID controller was tuned regarding several application scenarios, and its final parameters were determined based on the comprehensive control performance among multiple test conditions. The related performance results have been published in our previous work.[6] The NMPC basically shares the same setups as MMPC, except for the adjustments in manipulated variable's upper bound and the penalty coefficients. The adjustments were found necessary due to the major change in the predicted transient response.

Remark 2

Theoretically, multiple PID controllers can be employed to improve the single PID controller's performance, similar to the fact that MMPC outperforms MPC by taking advantage of the system dynamics in multiple operating points. However, PID is not equipped with the advantages in MPC, such as, constraints handling and optimization. We therefore believe that the multiple-PID control scheme might not observably boost the control performance, while its advantage of simplicity is compromised due to the increasing complexity. Therefore, the comparison between multi-PID control and MMPC is considered of limited value, and the further investigation is unnecessary.

4.2.1. Step-Change Setpoint Tracking. Figure 7 displays the results of the step-change setpoint tracking test. The simulation starts at the steady state of $DNI = 850\ W/m^2$, $N = 120$ krpm, and $TOT = 923$ K. In each *DNI* condition, namely, 850, 750, 650, and 550 W/m^2, a 1 krpm N_{set} step-change and a 30 K TOT_{set} step-change occur in sequence. Although the PID controller can perform smoothly under smaller N_{set} step-changes, it causes dangerous operating conditions, and the system pauses at the 1 krpm N_{set} step changes. To continue the control task, a rate limiter needs to be added between the N_{set}

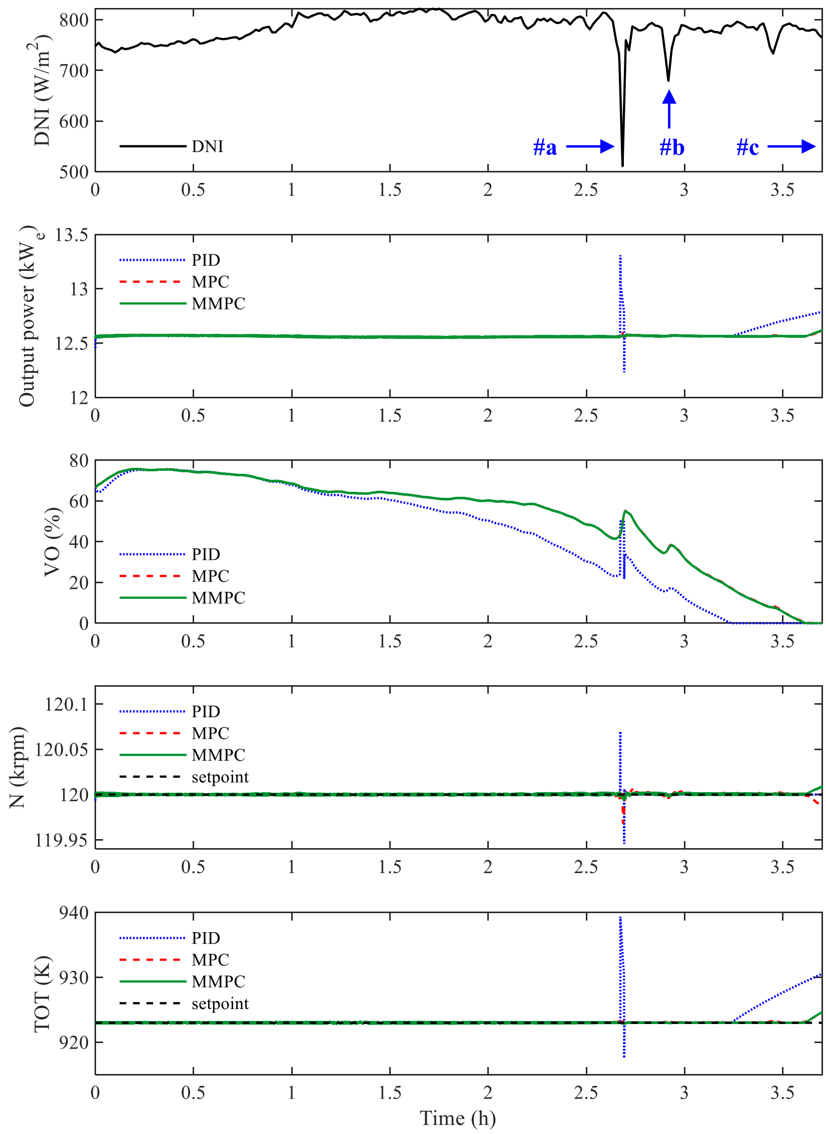

Figure 8. Transient response of design point operation under actual *DNI* (#a: the *DNI* drop at 2.7 h; #b: the *DNI* drop at 2.9 h; #c: the end of simulation; blue dotted line: PID; red dash line: MPC; green solid line: MMPC; and black dash line: output setpoints).

instruction and PID controller. However, for a fair comparison, the PID (blue) performance, as shown in Figure 7, is obtained without the rate limiter. The MPC, NMPC, and MMPC controllers, on the other hand, can still operate in benign conditions without any rate limiters. It can be observed intuitively that MMPC (green) causes smaller fluctuations and stabilizes more rapidly than MPC (red). The comparison between NMPC (blue) and MMPC, on the other hand, is more subtle. In general, the NMPC displays slightly smoother transitions and smaller overshoots than MMPC.

Table 2 summarizes the performance indicators for quantitative comparison between MPC, NMPC, and MMPC. Root-mean-square error (*RMSE*) indicates the overall setpoint tracking deviation during the whole simulation. The mathematical expectations (E) of the manipulated variables' increments and the overshoot values (OS) of the controlled variables evaluate the transient response performance.

In comparison with MPC, MMPC presents overall better setpoint tracking performance and smoother state transition, thanks to its higher prediction accuracy. MMPC follows the N_{set} and TOT_{set} more tightly under all *DNI* conditions, with average *RMSE* improvements of 0.059 krpm (33.74%) and 0.305 K (9.8%), respectively. MMPC also reduces the average overshoots of N and TOT by 0.232 krpm (29.03%) and 4.333 K (13.39%), respectively, which is an appreciable improvement. The average changing rate of the manipulated variables in MMPC is also 0.166 kW$_e$/s (42.24%) and 0.085%/s (10.98%) slower, respectively.

Nevertheless, the overall control performance is further improved in NMPC due to the superior prediction accuracy. The average *RMSE*s of NMPC are 0.020 krpm (17.46%) and 0.328 K (11.69%) lower than MMPC, respectively. The average overshoots of N and TOT are also 0.208 krpm (36.73%) and 8.868 K (31.64%) smaller, respectively. So are the improvements in output power and bypass valve opening's changing rates.

As a significant indicator in real-time control, the computing times of the optimization steps in NMPC and MMPC are also monitored. The average computing time in NMPC optimization is 1.90 s, which is 50 times longer than that of MMPC (0.04 s) and 19 times longer than the sampling time (0.1 s). Although the prediction horizon and control horizon are

https://doi.org/10.1021/acs.iecr.2c01784
Ind. Eng. Chem. Res. 2022, 61, 13532−13558

Table 3. Control Performance of Design Point Operation under Actual *DNI*[a]

Scenario	#a		#b		#c	
Parameter	e_N (krpm)	e_{TOT} (K)	e_N (krpm)	e_{TOT} (K)	e_N (krpm)	e_{TOT} (K)
PID	0.070	16.360	0.000	0.022	0.000	4.004
MPC	0.032	0.430	0.004	0.215	0.012	1.662
MMPC	0.006	0.129	0.002	0.027	0.009	1.655
MMPC's improvements over PID	**0.064**	**16.231**	**-0.002**	**-0.005**	**-0.009**	**2.349**
MMPC's improvements over MPC	**0.026**	**0.301**	**0.002**	**0.188**	**0.003**	**0.007**

[a]The data are displayed with three significant figures. *e* is the deviation from setpoint. MMPC's improvements = MPC/PID's value − MMPC's value. Green: positive improvements; and red: degressions.

already short enough, the computational speed of first-principle-model-based NMPC is still unable to satisfy the demand in real-time control.

In summary, the resultant response data indicate a generally more stable and smoother control performance of MMPC, compared with both PID and MPC. The control performance can be further enhanced by using NMPC. However, the slow computational speed hinders its implementation in real-time control.

4.2.2. Design Point Operation under Actual DNI Variation. The comparative discussion is further conducted in the design point operation under actual *DNI* variation. The *DNI* curve applied in this section is measured by the meteorological monitoring station on May 18th, 2017 on the solar power tower test site in Zhejiang University, Hangzhou, China, as displayed in Figure 8. The selected *DNI* data include small fluctuations and drastic changes, for example, the harsh drop at 2.7 h from 800 to 500 W/m^2 (#a in Figure 8) and the smaller drop from 780 to 680 W/m^2 (#b in Figure 8), which are caused by different degrees of realistic weather conditions. The control objective is to keep the *N* and *TOT* at their design value, that is, 120 krpm and 923 K, respectively. This allows the turbine to steadily operate in its optimum state, guaranteeing sufficient electricity generation and benign overall system performance. Such a high-performance operation requires a large amount of input energy, so the design point operation is only practical under high-DNI conditions.

As indicated in Figure 8 and Table 3, both MPC (red) and MMPC (green) can follow the setpoints with negligible deviations, namely, 0.032 krpm (0.03%) and 0.006 krpm (0.01%) in N_{set} tracking, respectively, and 0.430 K (0.05%) and 0.129 K (0.01%) in TOT_{set} tracking, respectively. With PID control (blue), however, there appears an apparent offset spike at situation #a. The sudden rises of 0.070 krpm (0.06%) in *N*, 16.360 K (1.77%) in *TOT* and 0.757 kW$_e$ (6.03%) in PW$_{out}$ would increase the risk of power grid instability, also detrimental to the turbine operation. This is related to the operation mode switching mechanism in PID control. When *DNI* drops to below 650 W/m^2, the constant *N* operation is triggered in case the power input and power release in TCES cannot sustain the design point operation (see ref 6). This might cause unnecessary instability during short-term climate changes. Such an issue can be better handled by MMPC where the mode switching is decided on the basis of multiple performance indicators and future operational states, thanks to the prediction models and optimizers. MMPC also outperforms MPC at situation #a with smaller deviations from the setpoints, thanks to the higher prediction accuracy.

The milder weather change at #b also causes some fluctuations as well. Unlike at #a, the deviations under MMPC control are slightly larger than PID. Because besides the mode switching part, the effect of *DNI* is not considered in PID control. Thanks to the larger thermal inertia of TCES, short-term, mild weather changes would not affect the control performance. However, the real-time measured *DNI* would affect the optimization result in each sampling period due to the embedded prediction model in MMPC. Nonetheless, the influence is very limited, and the tracking precisions are still satisfactory.

At the end of simulation (#c), the input solar energy gradually exceeds the system's capacity. *VO* reaches its lower limit, and all of the high-temperature air flows into TCES to store the excess thermal energy. When the TCES also reaches its full capacity, the turbine inlet temperature would be increased, and so would the *TOT*. As more energy cannot be stored in TCES, it needs to be used to generate electricity, which explains the gradual rise in output power. In this scenario, another advantage of MMPC stands out. That is, MMPC can prolong the design point operation by 25 min (13%) than PID. The *TOT* deviation is therefore obviously lower than that under PID control, reducing the risk of turbine overheating. Despite this, the N_{set} tracking accuracy of PID is still higher than MMPC's. The separate control loops in PID protect them from the influence of each other and hence enable faster dynamic response of *N*, yet at the cost of *TOT*'s performance. On the other hand, the multi-objective nature of MMPC requires the tradeoff between *N* and *TOT*'s responses. In spite of the small degression of e_N, the overall tracking performance is still better than PID.

In summary, for design point operation under actual *DNI* condition, MMPC generally presents higher control performance in setpoint tracking, operation stabilization, and avoidance of dangerous occasions than PID and MPC.

https://doi.org/10.1021/acs.iecr.2c01784
Ind. Eng. Chem. Res. 2022, 61, 13532−13558

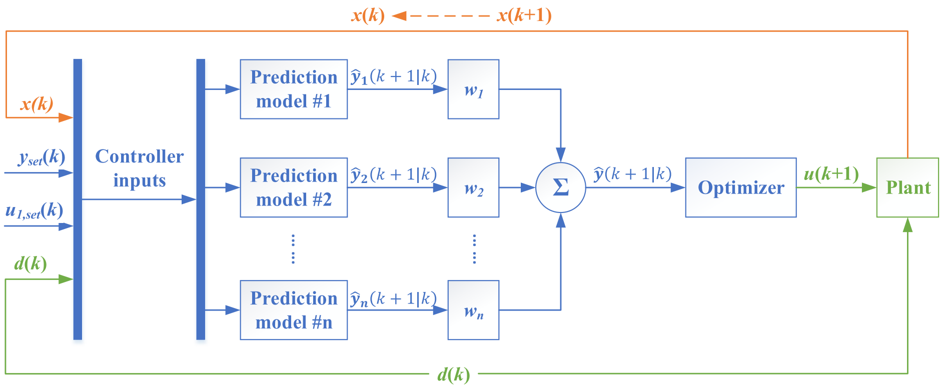

Figure 9. Schematic of MMPC control for power demand tracking (blue: MMPC controller; green: plant model; and orange: setpoints. The dash line indicates the state transition between the adjacent time steps).

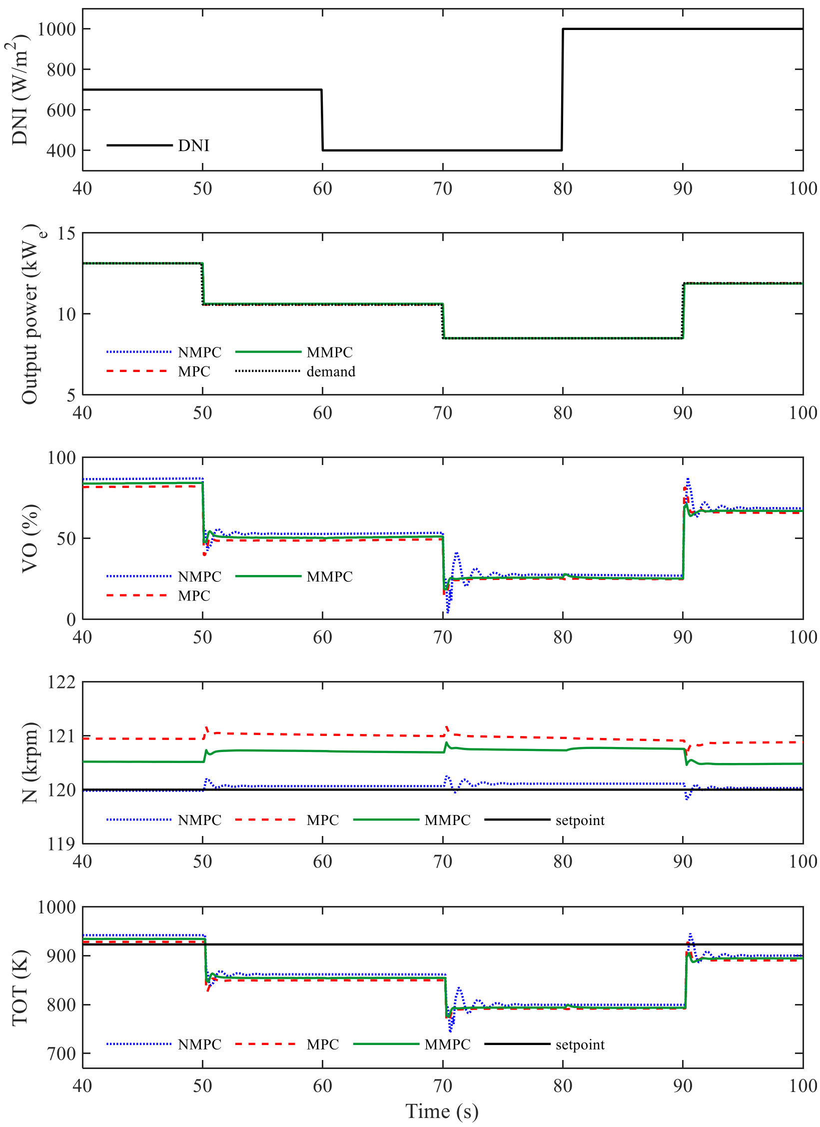

Figure 10. Transient response of step-change power demand tracking (black solid line: *DNI*, setpoints; black dotted line: power demand; blue dotted line: NMPC; red dash line: MPC; and green solid line: MMPC.)

5. POWER DEMAND TRACKING CONTROL

Given that the presented power system is a grid-connected solar power plant, besides the operation stability in specific working condition, the ability of responding to the power demand from the load dispatch center is of utmost significance as well. In this section, the MMPC controller is extended to fulfill the power demand, exploiting the dispatchability potential of the TCES-based solar air turbine system. The

https://doi.org/10.1021/acs.iecr.2c01784
Ind. Eng. Chem. Res. 2022, 61, 13532−13558

Table 4. Overall Control Performance of Power Demand Tracking[a]

Method	$RMSE_N$ (krpm)	$RMSE_{TOT}$ (K)	$RMSE_{PW_{out}}$ (kW$_e$)
MPC	0.961	88.282	0.193
NMPC	0.080	80.948	0.193
MMPC	0.663	85.584	0.193
MMPC VS MPC	**0.298**	**2.698**	**0.000**
MMPC VS NMPC	**-0.583**	**-4.636**	**0.000**

[a]The data are displayed with three significant figures. RMSE is the root-mean-square error. MMPC's improvements = MPC/NMPC's value − MMPC's value. Green: positive improvements and red: degressions.

Table 5. Control Performance of Power Demand Tracking under Different *DNIs*[a]

DNI	Method	OS_N (krpm)	OS_{TOT} (K)	Settling time (s)	Settling time (s)
700 W/m^2	MPC	0.124	22.947	2.0	1.1
	NMPC	0.144	25.873	4.6	2.7
	MMPC	0.006	7.281	2.1	1.1
	MMPC VS MPC	**0.118**	**15.666**	**-0.1**	**0.0**
	MMPC VS NMPC	**0.138**	**18.592**	**2.5**	**1.6**
400 W/m^2	MPC	0.190	25.313	2.3	1.0
	NMPC	0.143	56.719	6.9	4.9
	MMPC	0.133	18.451	2.1	0.8
	MMPC VS MPC	**0.057**	**6.862**	**0.2**	**0.2**
	MMPC VS NMPC	**0.010**	**38.268**	**4.8**	**4.1**
1000 W/m^2	MPC	0.262	37.835	3.4	1.5
	NMPC	0.220	45.388	5.8	3.8
	MMPC	0.016	10.737	2.7	1.4
	MMPC VS MPC	**0.246**	**27.098**	**0.7**	**0.1**
	MMPC VS NMPC	**0.204**	**34.651**	**3.1**	**2.4**
Average	MPC	0.192	28.698	2.6	1.2
	NMPC	0.169	42.660	5.8	3.8
	MMPC	0.052	12.156	2.3	1.1
	MMPC VS MPC	**0.140**	**16.542**	**0.3**	**0.1**
	MMPC VS NMPC	**0.117**	**30.504**	**3.5**	**2.7**

[a]The overshoot and settling time data are displayed with three and one significant figures, respectively. *OS* is the overshoot. Settling time refers to the duration between step changes happen until the changing rates of *N* or *TOT* are less than 0.01 krpm/s and 10 K/s, respectively. MMPC's improvements = MPC/NMPC's value − MMPC's value. Green: positive improvements; and red: degressions.

controller's performance is then discussed under step-change and actual power demand variations, respectively.

5.1. MMPC for Power Demand Tracking. To achieve the power demand tracking control, the system output power should keep up with the dispatching command, which is equivalent to the output power "setpoint" in MMPC. Thus, an additional penalty is considered in the objective function to minimize the deviation of PW_{out} from the demanded output power, PW_{dm}.

$$\begin{aligned} \min J(k) = &\left\|\boldsymbol{y}_{\mathbf{set,cor}}(k) - \hat{\boldsymbol{y}}_{\mathbf{cor}}(k)\right\|_{\boldsymbol{Q}}^2 + \|\Delta \boldsymbol{u}(k)\|_{\boldsymbol{R}}^2 \\ &+ \|\boldsymbol{u}_{\boldsymbol{1},\boldsymbol{set}}(k) - \boldsymbol{u}_{\boldsymbol{1}}(k)\|_{\boldsymbol{Q}_{u_1}}^2 \\ \text{s. t. } &\boldsymbol{x}(k+1) = \boldsymbol{A}\boldsymbol{x}(k) + \boldsymbol{B}_u\boldsymbol{u}(k) + \boldsymbol{B}_d d(k) \\ &\boldsymbol{y}(k) = \boldsymbol{C}\boldsymbol{x}(k) \\ &\boldsymbol{u}_{\boldsymbol{min}} \le \boldsymbol{u}(k) \le \boldsymbol{u}_{\boldsymbol{max}} \end{aligned} \tag{14}$$

https://doi.org/10.1021/acs.iecr.2c01784
Ind. Eng. Chem. Res. 2022, 61, 13532−13558

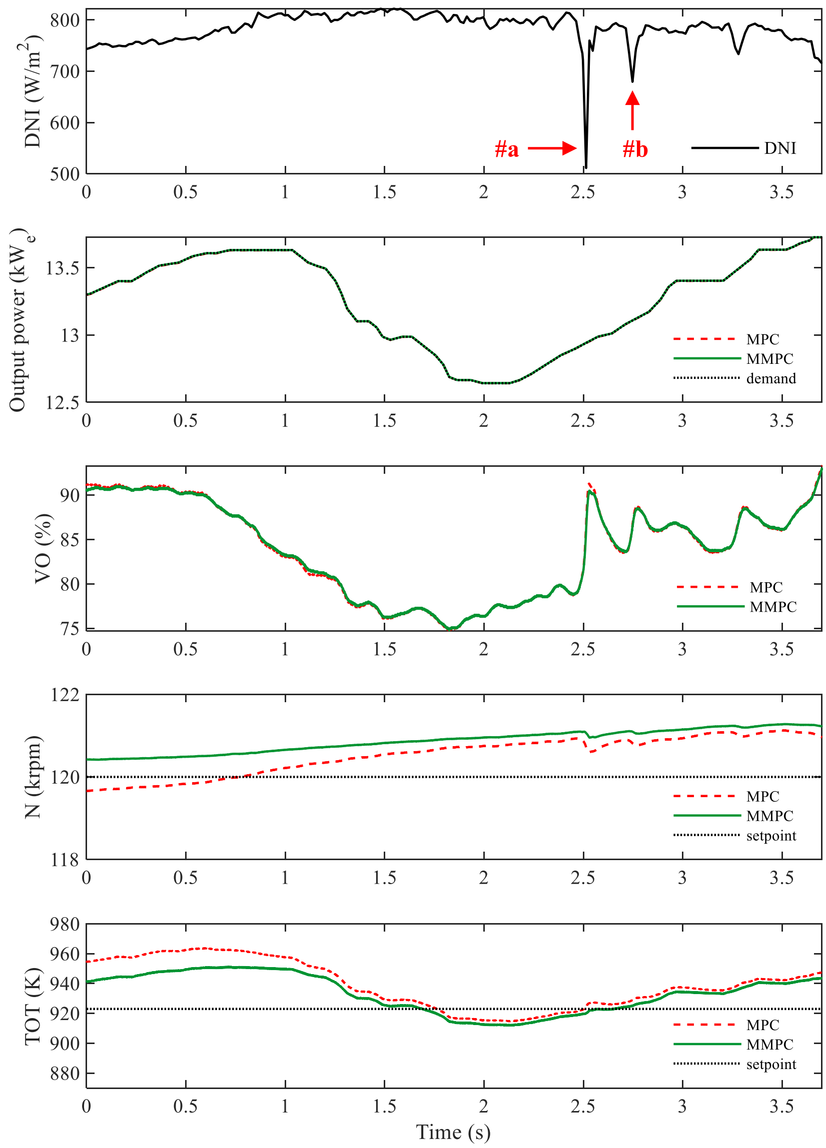

Figure 11. Transient response of actual power demand tracking under actual *DNI* variation (#a: the *DNI* drop at 2.5 h; #b: the *DNI* drop at 2.75 h; red dash line: MPC; green solid line: MMPC; and black dash line: power demand and output setpoints).

where $\boldsymbol{u}_{1,\mathrm{set}}$ refers to the demanded output power, PW_{dm}, given by the load dispatch center, $\boldsymbol{u}_1$ refers to the output electrical power, PW_{out}, and $\mathbf{Q}_{\mathrm{u1}}$ is the penalty coefficient for power demand tracking, $\mathbf{Q}_{\mathrm{u1}} = diag[q_{\mathrm{u1}}(1), ..., q_{\mathrm{u1}}(P)]$. When the need for power demand tracking comes to the priority, the $\mathbf{Q}_{\mathrm{u1}}$ value should be increased.

Since the reference trajectory tracking control of *TOT* and *N* depends on the regulation of PW_{out}, there are some tradeoffs to be made to accomplish power demand trajectory tracking. If both the electricity generation and consumption simultaneously vary in different patterns, the turbine can barely fix at a specific working state, even with the help of TCES. Efforts have been made to allow the output power to follow the power demand directly and immediately, ending up with the highly unstable and dangerous turbine operation. Therefore, in this case, the *TOT* and *N* setpoint tracking performances are compromised, and their prediction and control feedback corrections are no longer needed, as illustrated in Figure 9. Only the feedback correction of using real-time measured state variables as the initial prediction state is conserved in power demand tracking MMPC. Nonetheless, thanks to the comprehensive consideration in the objective function, as long as the penalty coefficients are reasonably tuned, *TOT* and *N* would not deviate from their setpoints too far away, so the turbine would still operate with high efficiency and stability.

This application highlights the advantages of MMPC control over the PID control. Because the output power is one of the manipulated variables, PID controllers are not able to track the power demand while maintaining *N* at its setpoint. In MMPC, the setpoint tracking and power demand fulfilling performances are comprehensively considered in the objective function. Both control targets would be satisfied if the condition permits. Otherwise, when there is an urgent need of load dispatch, the power demand response would be guaranteed first with allowable violations of setpoint tracking.

5.2. Case Study. In this section, the MMPC power demand control is verified in comparison with MPC and NMPC under different scenarios. The step-change power demand tracking scenario is designed to examine its ability to handle extreme situations. The actual power demand tracking

https://doi.org/10.1021/acs.iecr.2c01784
Ind. Eng. Chem. Res. 2022, 61, 13532−13558

Table 6. Control Performance of Power Demand Tracking[a]

Method	$RMSE_N$ (krpm)		$RMSE_{TOT}$ (K)	$RMSE_{PW_{out}}$ (kW$_e$)
MPC	0.710		22.615	0.002
MMPC	0.919		16.713	0.001
MMPC VS MPC	**-0.209**		**5.902**	**0.001**
Method	*N* fluctuation at #a (krpm)	*TOT* fluctuation at #a (K)	*N* fluctuation at #b (krpm)	*TOT* fluctuation at #b (K)
MPC	0.325	3.768	0.125	2.533
MMPC	0.140	2.194	0.054	1.172
MMPC VS MPC	**0.185**	**1.574**	**0.071**	**1.361**

[a]The data are displayed with three significant figures. *RMSE* is the root-mean-square error. MMPC's improvements = MPC's value − MMPC's value. Green: positive improvements and red: degressions.

under actual *DNI* variation then demonstrates the controller's capability of confronting disturbance and uncertainties. Different from the regulatory control, the NMPC in power demand tracking shares the same penalty coefficients with MMPC.

5.2.1. Step-Change Power Demand Tracking. The system inputs and the resultant transient responses of MPC, NMPC, and MMPC are displayed in Figure 10. The simulation starts at PW_{dm} = 13 kW$_e$ followed by three PW_{dm} step changes, namely, two 20% drops and one 40% rise, and two *DNI* step changes, namely, one 300 W/m^2 (43%) drop and one 600 W/m^2 (250%) rise. Each step change lasts for 10 s. TOT_{set} and N_{set} stay at their setpoints during the whole simulation.

Since the power demand tracking is the priority in this case and the output power itself is the manipulated variable, the output power can track the demand curve rapidly and precisely. In all the MPC (red), NMPC (blue), and MMPC (green) cases, the output electrical power reaches the power demand with less than 0.1% deviation in less than 0.5 s, and the fluctuations in the other performance parameters are mostly eliminated within 2 s after the step changes.

The response patterns in MPC and MMPC are of high similarity, while NMPC presents obvious oscillations during state transitions. Another observable difference lies in the tracking precisions of *N*. *N* is the closest to its setpoint under NMPC control, and MMPC comes second. This indicates that NMPC and MMPC can lower the risk of overspeed without significantly sacrificing other system performances.

The quantitative control performances of the three control targets are concluded in Tables 4 and 5. The *RMSE* values of MMPC are generally lower than MPC's and yet, larger than NMPC's. Compared with MPC, there are a 0.298 krpm (30.97%) and a 2.698 K (3.06%) improvements in the RMSE of *N* and *TOT*, respectively. When compared with NMPC, there are a 0.583 krpm and a 4.636 K degressions in the RMSE of *N* and *TOT*, respectively. Since the parameters settings are basically the same in each controller except for the prediction models, the advanced performance should be credited to the higher prediction accuracy in NMPC and MMPC.

To quantify the oscillation phenomenon in NMPC, the overshoots and settling times under different *DNI*s are summarized in Table 5. The MMPC presents the best steadiness in general. In some cases, NMPC's performance is even inferior to MPC. The average overshoots of *N* and *TOT* in MMPC are 0.117 krpm (69.43%) and 30.504 K (71.50%) smaller than NMPC, respectively. MMPC's settling times are also the shortest, that is, 2.3 and 1.1 s in *N* and *TOT*, respectively, which are 3.5 s (60.12%) and 2.7 s (71.05%) shorter than NMPC, respectively.

Furthermore, in terms of the computational speed, the average computing time of optimization in NMPC is 2.34 s. This is even longer than regulatory control due to the more complicated objective function. In contrast, the average computing time in MMPC is only 0.06 s, proving stronger practicability in real-time control.

Overall, the setpoint tracking and operation risk prevention of MMPC are generally better than MPC in step-change power demand tracking under step-change *DNI* conditions. Moreover, when compared with NMPC, MMPC shows slightly poorer setpoint tracking accuracies but more steady and faster state transitions.

5.2.2. Actual Power Demand Tracking under Actual DNI Variation. The power demand tracking performance is further studied under actual power demand curve and actual *DNI* variation. As shown in Figure 11, the *DNI* variation is the same data as shown in Section 4.2.2. The corresponding power demand curve is originated from the typical power demand curve on weekdays (the *DNI* data is collected on Thursday) in Hangzhou, China and carefully scaled to match the 10 kW$_e$ plant in this study.

The results in Figure 11 and Table 6 show similar statistical regularity to those in Section 5.2.1. During the whole simulation, the output power deviations from the demanded value are no more than 0.003 kW$_e$ (0.02%). The MMPC controller (green) can precisely track the power demand with 0.001 kW$_e$ RMSE, which is 50% lower than MPC's (red). Although the *N* in MMPC slightly deviates more than MPC by 0.209 krpm (29.49%), the TOT deviation is 5.902 K (26.10%) smaller than that in MPC. The same trend can be intuitively observed in Figure 11. Despite the same control parameters settings, MMPC and MPC end up with different tradeoff decisions. This can be settled by adjusting the penalty coefficients in eq 14.

During the DNI decrease at #a, the *N* and *TOT* fluctuations caused by MMPC are 0.185 krpm (56.92%) and 1.574 K (41.77%) lower than MPC, respectively. The same trend goes for the fluctuations at #b with a 0.071 krpm (56.80%) and a 1.361 K (53.73%) reduction, respectively. The stronger ability of resisting disturbances in MMPC can be explained by its better predictive performance.

https://doi.org/10.1021/acs.iecr.2c01784
Ind. Eng. Chem. Res. 2022, 61, 13532−13558

In summary, MMPC and MPC present various advantages in target tracking, while MMPC outperforms MPC in system stabilization in actual power demand tracking under actual *DNI* variation.

6. DISCUSSION

6.1. Closed-Loop Stability Evaluation. Due to the high complexity of the system dynamics and numerical modeling

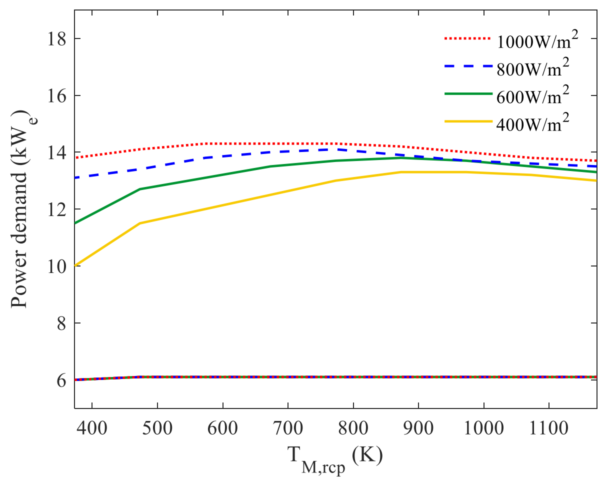

Figure 12. Stable zone of varied recuperator core temperatures.

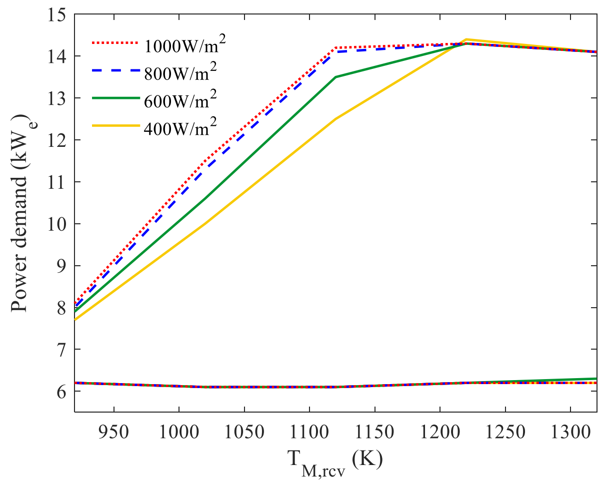

Figure 13. Stable zone of varied receiver core temperatures.

technique, it is difficult to perform theoretical evaluations on the controller's closed-loop stability. Experiments need to be carried out to determine the practical stability region and to ensure the controller is working within. Besides, algorithms such as boundary control[68,69,72,73] could be incorporated to further improve the stability of such a control scheme.

In principle, the risk of dangerous operation mainly lies in turbomachinery components due to their fastest and most sensitive dynamics. As demonstrated in Figure 2, the operation states should avoid the dangerous surging and choking conditions, which are beyond the areas where the solid lines cover. Moreover, during actual operation, the working states are expected to be close to the colored points, as shown in Figure 2. In other words, according to turbomachinery theory, the area that the solid lines cover, especially where close to the dash lines, can be regarded as the stable operation zones. So far, all the operation states obtained in the current work are within the stable operation zones.

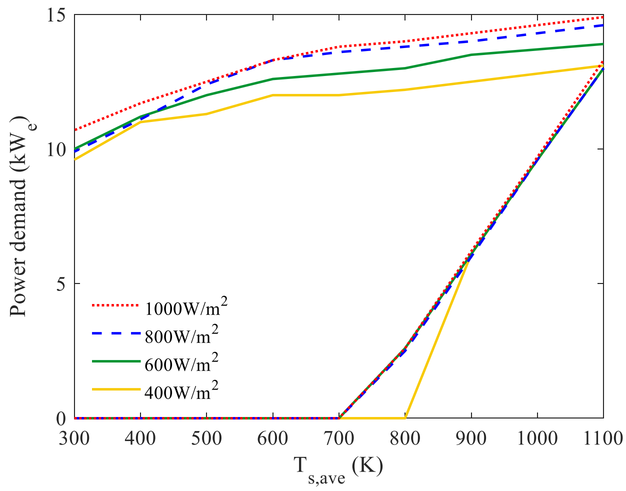

Figure 14. Stable zone of varied average temperature of storage medium.

Table 7. Parameters of the Measurement Noise and the First-Order Filter[a]

measured parameter	measuring precision (%)	noise amplitude	noise power	filter's time constant (s)
TOT	±0.5	<6 K	0.3	3
N	±0.1	<0.1 krpm	0.0001	1
P_2	±0.5	<1 kPa	0.01	1
$T_{M,rcp}$	±0.5	<4 K	0.1	1
$T_{M,rcv}$	±0.5	<6 K	0.3	1
$T_{g,ave}$	±0.5	<6 K	0.3	1
$T_{s,ave}$	±0.5	<6 K	0.3	1

[a]The measuring precisions are derived from the sensors' manufacturing information.

Additionally, to further quantify the closed-loop stability, extra tests have been conducted to explore the boundaries of the stable zone of some critical parameters. The power demand tracking MMPC is taken as an example. The main disturbances come from the power demand and DNI. Important state variables include the core temperature of the recuperator, $T_{M,rcp}$, the core temperature of the receiver, $T_{M,rcv}$, and the average solid temperature in TCES, $T_{s,ave}$. From an engineering perspective, these temperature states impose relatively larger influence on system dynamics as they are normally of very high values and represent the energy level of the whole system. Thus, the boundary tests are conducted with different values of $T_{M,rcp}$, $T_{M,rcv}$, and $T_{s,ave}$ under different DNIs.

To perform the test, simulation starts at a certain steady state and transits to another one under the action of the MMPC controller. When the system fails to turn into stable operation and last for least 1 min, this condition is considered unstable. Situations occur when system turns stable but then the valve opening slowly approaches its physical limits due to the large inertia of TCES. Once its physical limits are reached, the valve opening is no longer able to control the system, which would eventually drive the system into instability. Thus, a 1 min threshold time duration is proposed, which should be adequate for the operators to notice the situation and adjust the control instructions in time. Additionally, to present the results in an organized manner, the control variable method is

https://doi.org/10.1021/acs.iecr.2c01784
Ind. Eng. Chem. Res. 2022, 61, 13532−13558

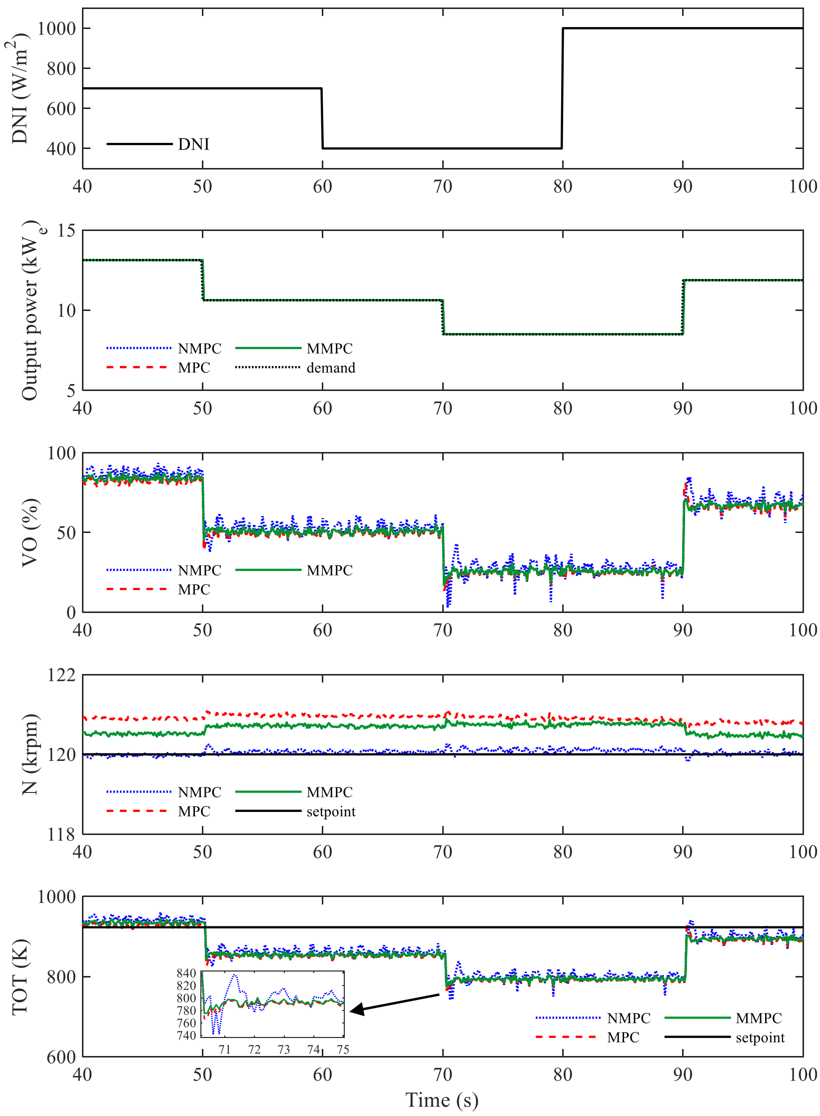

Figure 15. Transient response of step-change power demand tracking with measurement noises.

employed. When one of the $T_{M,rcp}$, $T_{M,rcv}$, and $T_{s,ave}$ is varied, the other two variables stay constant.

The resultant stable zones are displayed in Figures 12−14. In general, as *DNI* gets higher, the stable zone gets wider, which mainly reflects in the upper boundary of power demand. The larger amount of energy input enables the system to generate more electricity power.

The increasing trend of the lower boundary of $T_{s,ave}$'s stable zone (Figure 14) can also be explained by energy conservation. The *DNI* and storage medium's temperature decide the outlet temperatures of receiver and TCES unit, respectively. The window between receiver's and TCES's outlet temperatures decides the flexibility of *TIT* and, therefore, the turbine's ability of power generation. When the $T_{s,ave}$ is of high value, it is not possible to lower down *TIT* and hence the output power. Eventually, the stable operation zone in high $T_{s,ave}$ narrows down.

As shown in Figures 12 and 13, the lower boundaries are almost the same with different *DNI*s and core temperatures of the recuperator and receiver. Experience showed that the upper and lower limits of power demand correspond to the upper and lower limits of TCES bypass valve opening, respectively. In the case of the upper limit, the TCES unit is fully bypass, and it cannot be used to adjust the *TIT*. In the case of lower limit, all the air flows into TCES. The *TIT* and output power would remain unchanged in a short period as it is decided by the storage medium's temperature, which stays constant in Figures 12 and 13.

Overall, the examined boundaries of the stable operation zone are mainly affected by the physical limitations of the TCES bypass valve opening. The results showed that within these stable zones, the proposed MMPC controller can achieve its control objectives without causing unstable operation of system components.

6.2. Performance Evaluation with Measurement Noises. Measurement noise is an important factor in practical applications. In this section, performance evaluation under realistic measurement noises is conducted on the MMPC, MPC, and NMPC controllers. Regarding the fact that the responsive curves might bring difficulty to distinguish different controllers' performances, the performance with measurement noises is discussed separately in this section.

The band-limited white noise module and the first-order filter module in Simulink are used to imitate the measurement

https://doi.org/10.1021/acs.iecr.2c01784
Ind. Eng. Chem. Res. 2022, 61, 13532−13558

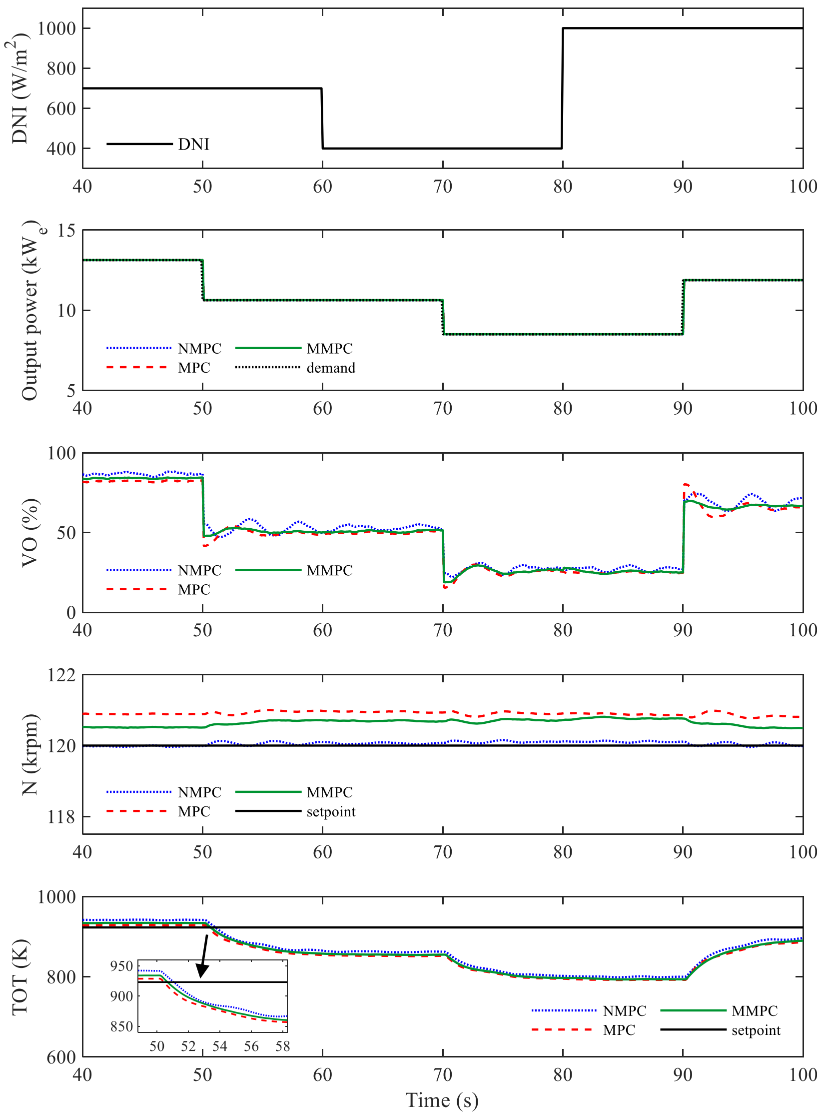

Figure 16. Transient response of step-change power demand tracking with measurement noises and first-order filters.

noises and reduce their influence on the control performance, respectively. Table 7 lists the parameter settings of the noises and filters. All the feedback parameters are treated with measurement noises and filters. The noise powers are selected according to the operation ranges of the measured parameters and the measuring precisions of the sensors, namely, thermocouple, pressure transducer, and rotational speed transducer. The time constants of the first-order filters are tuned individually.

To investigate the performance under the measurement noises and filters, both filtered and unfiltered cases are simulated under the power demand tracking scenario, as shown in Figures 15 and 16.

In the unfiltered case (Figure 15), the additional noises resulted in observable fluctuations in *N* and *TOT*. Among the three controllers, NMPC presents the most fluctuations. At about 71 s, *TOT* increased 95 K, while in MPC and MMPC cases, *TOT* only varied 22 K. Plus, the overshoot values caused by MMPC are slightly smaller than by MPC, for example, 10 K smaller during the state transition after 70 s.

The fluctuations caused by the measurement noises can be reduced by adopting first-order filters (Figure 16). The addition of filters not only removed most of the fluctuations but also caused improved responsive performance in *TOT*. Although the settling time was prolonged to about 10 s, the state transition curves were greatly smoothened with the overshoots basically eliminated. Among the three controllers, MMPC presented the best smoothness, while NMPC showed the highest tracking precision.

7. CONCLUSIONS

In this paper, a multi-MPC (MMPC) scheme is designed for a solar power system with microturbine and TCES. Conventionally, the gas turbine control is undertaken by PID controllers because of their robustness and reliability. A PID control strategy is previously developed for the TCES-based solar air turbine system control. However, PID control has its limitations in the multi-variable control of the coupled system. MPC is therefore proposed to take care of the constrained multi-variable control in different scenarios by offering the optimal open-loop solutions in each sampling time. A multi-modeling method is proposed by taking advantage of the close relationship between *DNI* and system states, adding to the practical value in the CSP industry application. The prediction

https://doi.org/10.1021/acs.iecr.2c01784
Ind. Eng. Chem. Res. 2022, 61, 13532−13558

models are identified as linear state-space models from the first-principle nonlinear model with more than 95% accuracies. Feedback correction is carefully designed in three aspects, including the corrections of (1) the prediction initial states, (2) the predicted output errors, and (3) the setpoint tracking deviations. After feedback corrections, the N and TOT tracking errors are all reduced to <0.01%.

The controllers' performances are first studied in regulatory control where MMPC demonstrates superior performances than PID control in multiple aspects. In step-change setpoint tracking, MMPC presents stronger adaptability to the changes in N_{set} than PID and shows generally higher tracking accuracies and stability than MPC. Although the control performance can be further enhanced by using NMPC, the much larger computational burden brings down its practicability in real-time control. Controllers' practicability is also comparatively investigated in design point operation under actual DNI variation. When DNI drops from 800 to 500 W/m^2, PID exposes its inferiority by switching to constant N operation mode and causing a 16.360 K (1.77%) deviation in TOT, while there are no evident fluctuations in MMPC curves. MMPC also prolongs the design point operation by 13% compared to PID. Moreover, in the presence of sudden DNI changes, the performance fluctuations in MMPC are generally smaller than those in MPC.

To meet the requirements of practical applications, MMPC is extended for power demand tracking by adjusting the objective function to consider the deviation of output power from the power demand. As the power tracking comes to the priority, feedback corrections for N_{set} and TOT_{set} tracking are no longer needed. When the power demand varies in the step-change pattern, the output power deviation can reduce to <0.1% in less than 0.5 s. When tracking the actual power demand, the deviations are no more than 0.02%. Besides, even VO becomes the only remaining manipulated variable, N and TOT still stay close to their setpoints, keeping the turbine operating in high-efficiency conditions. MMPC also shows stronger ability of resisting disturbances than MPC and more steady and faster state transitions than NMPC. More importantly, such an application scenario cannot be achieved by PID control where the output power works as a manipulated variable in this case.

In conclusion, the proposed MMPC control scheme can provide satisfactory performance in setpoint tracking and disturbance resisting applications and can effectively realize the power-demand-tracking function of the solar power system with microturbine and TCES. From the application perspective, the proposed MMPC design method has a high practical value and require low effort to implement in the CSP industry.

■ APPENDIX

A. Mathematical Model of the Solar Power System with Microturbine and TCES

The MATLAB/Simulink model of the studied system consists of three different types of component models, namely, the turbomachinery, the heat exchanger, and the power electronics models. The first-principle model involves the use of interpolation/table-lookup calculations (in compressor and turbine models), iterative solutions (in the receiver model), complex nonlinear empirical equations (in receiver and TCES models), and finite element modeling (in the TCES model).

A.1. Turbomachinery. The turbomachinery components include the compressor and the turbine. Their outlet temperatures are calculated as below.

$$T_{02} = T_{01}\left(1 + \frac{PR^{\gamma-1/\gamma} - 1}{\eta_c}\right) \tag{15}$$

$$T_{06} = T_{05}\left[1 - \eta_t\left(1 - \frac{1}{ER^{\gamma-1/\gamma}}\right)\right] \tag{16}$$

where T is the temperature, the subscripts 01, 02, 05, and 06 refer to the compressor inlet, compressor outlet, turbine inlet, and turbine outlet, respectively; PR and ER are the compressor pressure ratio and turbine expansion ratio, respectively; η is the isentropic efficiency, the subscripts c and t refer to compressor and turbine, respectively; γ is the ratio of air-specific heat at a constant pressure and a constant volume. Thereinto, PR, ER, and η are obtained through linear interpolation from the performance maps of compressor and turbine, for example, the maps shown in Figure 2.

The outlet pressures of the compressor and turbine are calculated according to the definition of PR and ER.

The works consumed by compressor and produced by turbine are calculated as below

$$PW_c = \dot{m}_c(h_{02} - h_{01}) \tag{17}$$

$$PW_t = \dot{m}_t(h_{05} - h_{06}) \tag{18}$$

where PW is the mechanical work; $\dot{m}$ is the mass flow rate, it is also obtained via linear interpolation from the performance maps; and h is the enthalpy, it is a function of the airflow temperature.

A.2. Heat Exchangers. The heat exchanger components include the recuperator, the receiver, and the TCES unit.

A.2.1. Recuperator. The recuperator parameters are calculated according to the energy conservation rule using the lumped-volume method.

$$MC_{p,M}\frac{dT_M}{dt} = \dot{Q}_h - \dot{Q}_c \tag{19}$$

$$\dot{Q}_h = \dot{m}_h C_{p,h}(T_{h,in} - T_{h,out}) = U_h A_h\left(\frac{T_{h,in} + T_{h,out}}{2} - T_M\right) \tag{20}$$

$$\dot{Q}_c = \dot{m}_c C_{p,c}(T_{c,out} - T_{c,in}) = U_c A_c\left(T_M - \frac{T_{c,in} + T_{c,out}}{2}\right) \tag{21}$$

where M is the total mass of the heat-transfer core; the subscript M refers to the heat-transfer core; C_p is the specific heat, the subscripts h and c refer to the hot side and the cold side, respectively; $\dot{Q}$ is the convective heat-transfer flux, the subscripts in and out refer to the inlet and outlet of the recuperator; U is the convective heat-transfer coefficient; and A is the convective heat-transfer area. The values of the thermophysical parameters are provided by the manufacturer.

A.2.2. Receiver. The receiver parameters are calculated by the energy conservation rule using the lumped-volume method. The thermophysical properties involved in the equations below are determined by the local temperature and pressure, and they are calculated through iteration.

https://doi.org/10.1021/acs.iecr.2c01784
Ind. Eng. Chem. Res. 2022, 61, 13532−13558

$$MC_{p,\mathrm{M}}\frac{\mathrm{d}T_{\mathrm{M}}}{\mathrm{d}t} = \dot{Q}_{\mathrm{in}} - \dot{Q}_{\mathrm{loss}} - \dot{Q}_{\mathrm{use}} \tag{22}$$

$$\dot{Q}_{\mathrm{in}} = \mathrm{DNI}\cdot A_{\mathrm{mir}}\cdot\eta_{\mathrm{field}} \tag{23}$$

$$\dot{Q}_{\mathrm{loss}} = (U_{\mathrm{ar}}A_{\mathrm{ar}} + U_{\mathrm{ac}}A_{\mathrm{ac}} + U_{\mathrm{r}}A_{\mathrm{r}} + U_{\mathrm{z}}A_{\mathrm{z}})(T_{\mathrm{wicav}} - T_{\mathrm{amb}}) \tag{24}$$

$$\dot{Q}_{\mathrm{use}} = \dot{m}C_{p,\mathrm{m}}(T_{\mathrm{out}} - T_{\mathrm{in}}) = h_{\mathrm{conv}}A_{\mathrm{conv}}\left(T_{\mathrm{M}} - \frac{T_{\mathrm{in}} + T_{\mathrm{out}}}{2}\right) \tag{25}$$

where M is the lumped mass of the receiver's core; A_{mir} is the total area of the heliostat mirrors in use; η_{field} is the heliostat field efficiency; the subscripts in, loss, and use refer to the incident solar irradiance, the thermal loss, and the energy which is absorbed by the airflow, respectively; the subscripts ar, ac, r, and z refer to the radiative loss through aperture, the convective loss through aperture, the thermal loss through the radial direction, and the thermal loss through the receiver's bottom, respectively; T_{M}, T_{wicav}, and T_{amb} refer to the lumped mass's temperature, the internal wall temperature of cavity, and the ambient air's temperature, respectively; and h_{conv} and A_{conv} are the convective heat-transfer coefficient and area, respectively.

Thereinto, U_{ar} is calculated as below

$$U_{\mathrm{ar}} = \frac{Nu_{\mathrm{ar}}k_{\mathrm{air}}}{D_{\mathrm{icav}}} \tag{26}$$

$$Nu_{\mathrm{ar}} = 0.000154Gr^{0.627}(2 + \cos\phi)^{-1.054}(1 + \varepsilon_{\mathrm{p}})^{0.313}A\,R^{1.638} \tag{27}$$

$$Gr = \frac{L_{\mathrm{icav}}^{3}g\beta(T_{\mathrm{wicav}} - T_{\mathrm{amb}})}{\upsilon_{\mathrm{air}}^{2}} \tag{28}$$

$$\varepsilon_{\mathrm{p}} = \left[\frac{(1-\varepsilon)/\varepsilon}{1 + 4(L_{\mathrm{icav}}/D_{\mathrm{icav}})} + 1\right]^{-1} \tag{29}$$

where Nu is the Nusselt number; k is the thermal conductivity; D_{icav} and L_{icav} are the inner diameter and the length of the cavity; Gr is the Grashof number; ϕ is the decline angle of the receiver; ε and ε_{p} are the emissivity and effective emissivity of the cavity; AR is the ratio of the aperture diameter over the cavity inner diameter; g is the gravitational acceleration; β is the reciprocal of the ambient temperature; and υ_{air} is the kinematic viscosity of the air.

U_{ac} is calculated as below

$$U_{\mathrm{ac}} = \frac{Nu_{\mathrm{ac}}k_{\mathrm{air}}}{D_{\mathrm{icav}}} \tag{30}$$

$$Nu_{\mathrm{ac}} = 0.088Gr^{1/3}\left(\frac{T_{\mathrm{wicav}}}{T_{\mathrm{amb}}}\right)^{0.18}(\cos\phi)^{2.47}\left(\frac{D_{\mathrm{icav}}}{L_{\mathrm{icav}}}\right)^{s} \tag{31}$$

$$s = 1.12 - 0.98\left(\frac{D_{\mathrm{icav}}}{L_{\mathrm{icav}}}\right) \tag{32}$$

$U_{\mathrm{r}}A_{\mathrm{r}}$ is calculated as below:

$$U_{\mathrm{r}}A_{\mathrm{r}} = \frac{1}{R_{\mathrm{itube}} + R_{\mathrm{gap}} + R_{\mathrm{etube}} + R_{\mathrm{isolr}} + R_{\mathrm{extr}}} \tag{33}$$

$$R_{\mathrm{itube}} = \frac{\ln(D_{\mathrm{eitube}}/D_{\mathrm{iitube}})}{2\pi k_{\mathrm{itube}}L_{\mathrm{tube}}} \tag{34}$$

$$R_{\mathrm{gap}} = \frac{\ln(D_{\mathrm{ietube}}/D_{\mathrm{eitube}})}{2\pi k_{\mathrm{air}}L_{\mathrm{tube}}} \tag{35}$$

$$R_{\mathrm{etube}} = \frac{\ln(D_{\mathrm{eetube}}/D_{\mathrm{ietube}})}{2\pi k_{\mathrm{etube}}L_{\mathrm{tube}}} \tag{36}$$

$$R_{\mathrm{isolr}} = \frac{\ln(D_{\mathrm{eisol}}/D_{\mathrm{eetube}})}{2\pi k_{\mathrm{isol}}L_{\mathrm{icav}}} \tag{37}$$

$$R_{\mathrm{extr}} = \frac{1}{\pi D_{\mathrm{eisol}}L_{\mathrm{ecav}}h_{\mathrm{extr}}} \tag{38}$$

where R is the thermal resistance; the subscripts itube, air, etube, and isol refer to the inner absorption tubes, the air between inner and outer tubes, the outer absorption tubes, and the insulation layer, respectively; the subscripts iitube, eitube, ietube, eetube, and eisol refer to the inner diameter of the inner tubes, the outer diameter of the inner tubes, the inner diameter of the outer tubes, the outer diameter of the outer tubes, and the outer diameter of the insulation layer, respectively; the subscripts tube, icav, and ecav refer to the lengths of the tubes, inner wall of insulation layer, and the outer wall of the receiver; and h_{extr} is the natural convective heat-transfer coefficient between the receiver's outer wall and the ambient air. It is calculated as below

$$h_{\mathrm{extr}} = \frac{Nu_{\mathrm{r}}k_{\mathrm{air}}}{D_{\mathrm{eisol}}} \tag{39}$$

$$Nu_{\mathrm{r}} = \left\{0.60 + \frac{0.387Ra^{1/6}}{[1 + (0.559/Pr)^{9/16}]^{8/27}}\right\}^{2} \tag{40}$$

$$Ra = \frac{g\beta(T_{\mathrm{eisolr}} - T_{\mathrm{amb}})D_{\mathrm{eisol}}^{3}}{\upsilon_{\mathrm{air}}^{2}}Pr_{\mathrm{air}} \tag{41}$$

where Ra is the Rayleigh number, Pr is the Prandtl number, and the subscript eisol refers to the outer diameter of the insulation layer.

$U_{\mathrm{z}}A_{\mathrm{z}}$ is calculated as below

$$U_{\mathrm{z}}A_{\mathrm{z}} = \frac{1}{R_{\mathrm{isolb}} + R_{\mathrm{extb}}} \tag{42}$$

$$R_{\mathrm{isolb}} = \frac{e_{\mathrm{isolb}}}{k_{\mathrm{isol}}A_{\mathrm{isolb}}} \tag{43}$$

$$R_{\mathrm{extb}} = \frac{1}{h_{\mathrm{extb}}A_{\mathrm{isolb}}} \tag{44}$$

where e is the thickness. Thereinto, h_{extb} is calculated as below

$$h_{\mathrm{extb}} = \frac{Nu_{\mathrm{z}}k_{\mathrm{air}}}{D_{\mathrm{isolb}}} \tag{45}$$

$$Nu_{\mathrm{z}} = 0.56(Gr\cdot Pr\cdot\cos\phi)^{1/4} \tag{46}$$

$$Gr = \frac{D_{\mathrm{isolb}}^{3}g\beta(T_{\mathrm{wisolb}} - T_{\mathrm{amb}})}{\upsilon_{\mathrm{air}}^{2}} \tag{47}$$

The h_{conv} in eq 25 is calculated as below

https://doi.org/10.1021/acs.iecr.2c01784
Ind. Eng. Chem. Res. 2022, 61, 13532−13558

$$Nu_{\mathrm{f}} = \frac{(f/8)(Re - 1000)Pr_{\mathrm{f}}}{1 + 12.7\sqrt{f/8}\,(Pr_{\mathrm{f}}^{2/3} - 1)}\left[1 + \left(\frac{d}{l}\right)^{2/3}\right]c_{\mathrm{t}} \quad (48)$$

$$f = (1.82\lg Re - 1.64)^{-2} \quad (49)$$

where f is the Darcy resistance coefficient of the inner tube turbulent flow; Re is the Reynolds number; d and l are the inner diameter and the length of the absorption tube, respectively; and c_{t} is calculated by the airflow temperature and tube wall temperature.

The frictional and local pressure losses are calculated as below

$$h_{\mathrm{f}} = \lambda\frac{l}{d}\frac{V^2}{2g}h \quad (50)$$

$$h_{\mathrm{j}} = \zeta\frac{V^2}{2g} \quad (51)$$

$$\lambda = \frac{0.3164}{Re^{1/4}} \quad (52)$$

where h_{f} and h_{j} refer to the frictional loss and the local loss, respectively; λ and ζ are the frictional and local loss coefficient, respectively; and V is the airflow velocity.

A.2.3. Thermochemical Energy Storage. The TCES model is built using the finite element method, so that the large thermal inertia and volumetric effect caused by its relatively large volume could be reflected in thermodynamic behavior.

The TCES's reactor core is divided into M elements along the flow direction. The energy conservation in the solid field can be expressed as below:

For the first element

$$M_iC_{p,\mathrm{M},i}\frac{\mathrm{d}T_{\mathrm{s},i}}{\mathrm{d}t} = \dot{Q}_{\mathrm{conv},i} + \dot{S}_{\mathrm{h},i} - \dot{Q}_{\mathrm{loss},i} - \dot{Q}_{\mathrm{cond},i} \quad (53)$$

For the second to the $(M-1)$th elements

$$M_iC_{p,\mathrm{M},i}\frac{\mathrm{d}T_{\mathrm{s},i}}{\mathrm{d}t} = \dot{Q}_{\mathrm{conv},i} + \dot{S}_{\mathrm{h},i} - \dot{Q}_{\mathrm{loss},i} + \dot{Q}_{\mathrm{cond},i-1} - \dot{Q}_{\mathrm{cond},i} \quad (54)$$

For the Mth element

$$M_iC_{p,\mathrm{M},i}\frac{\mathrm{d}T_{\mathrm{s},i}}{\mathrm{d}t} = \dot{Q}_{\mathrm{conv},i} + \dot{S}_{\mathrm{h},i} - \dot{Q}_{\mathrm{loss},i} + \dot{Q}_{\mathrm{cond},i-1} \quad (55)$$

In the fluid field, the energy conservation can be written as below:

For the first to the Mth elements

$$\rho_iA_{\mathrm{air},i}L_iC_{\mathrm{v},i}\frac{\mathrm{d}T_{\mathrm{m},i}}{\mathrm{d}t} = \dot{m}_iC_{p,i}T_{\mathrm{g},i} - \dot{m}_{i+1}C_{p,i+1}T_{\mathrm{g},i+1} - \dot{Q}_{\mathrm{conv},i} \quad (56)$$

where

$$\dot{Q}_{\mathrm{conv},i} = h_{\mathrm{conv},i}A_{\mathrm{conv},i}(T_{\mathrm{m},i} - T_{\mathrm{s},i}) \quad (57)$$

$$\dot{Q}_{\mathrm{cond},i} = k_iA_{\mathrm{s},i-1}\frac{T_{\mathrm{s},i} - T_{\mathrm{s},i+1}}{\mathrm{d}x} \quad (58)$$

$$\dot{S}_{\mathrm{h},i} = \Delta H_{\mathrm{r}}\cdot R_{\mathrm{t},i}\cdot C_{\mathrm{t},i} \quad (59)$$

When reduction reaction happens

$$R_{\mathrm{t},i} = k_{\mathrm{red},i}(1 - \alpha_i) - k_{\mathrm{oxi},i}\alpha_i \quad (60)$$

When oxidation reaction happens

$$R_{\mathrm{t},i} = k_{\mathrm{oxi},i}(1 - \alpha_i) - k_{\mathrm{red},i}\alpha_i \quad (61)$$

where i is the number of the element; the subscript s, g, and m refer to the solid field, the fluid field, and the average airflow; A_{conv} and A_{air} are the convective heat-transfer area and the cross-section area of the fluid field, respectively; k in eq 58 is the thermal conductivity; $\dot{S}_{\mathrm{h}}$ is the chemical reaction heat; ΔH_{r} is the standard molar reaction enthalpy; R_{t} is the reaction rate; C_{t} is the amount of substance of reactant; ρ is the airflow density; L is the length of the total storage medium's bulk; C_v is the specific heat of constant volume; k in eqs 60 and 61 is reaction rate constant, the subscript red and oxi refer to reduction and oxidation reactions, respectively; and α_{i} is the conversion rate.

The convective heat-transfer coefficient h_{conv} is calculated by

$$Nu = 3.66 + \frac{0.0668(d_{\mathrm{h}}/L)\cdot Re\cdot Pr}{1 + 0.04[(d_{\mathrm{h}}/L)\cdot Re\cdot Pr]^{2/3}} \quad (62)$$

The pressure loss in TCES is calculated as below

$$\Delta P = \frac{4fL}{d_{\mathrm{h}}}\frac{1}{2}\rho u_{\mathrm{m}}^2 \quad (63)$$

where ΔP is the pressure loss; f is the Fanning coefficient; L is the tube length; d_{h} is the hydraulic diameter; and u_{m} is the flow velocity.

A.3. Power Electronics. The power electronics components include the rotational shaft, a HSA, a rectifier, and an inverter.

The model is built according to the torque equilibrium as below

$$J\frac{\mathrm{d}\omega}{\mathrm{d}t} = \frac{1}{\omega}PW_{\mathrm{net}} \quad (64)$$

$$PW_{\mathrm{net}} = PW_{\mathrm{gt}} - PW_{\mathrm{load}}/\eta_{\mathrm{HSA}}\eta_{\mathrm{REC}}\eta_{\mathrm{INV}} \quad (65)$$

$$PW_{\mathrm{gt}} = PW_{\mathrm{t}} - PW_{\mathrm{c}}/\eta_{\mathrm{m}} \quad (66)$$

where J is the rotational mechanical inertia; ω is the angular velocity of the shaft; the subscripts net, gt, load, t, and c refer to the net power, the power outputted by gas turbine, the load power, the power produced by the turbine, and the power consumed by the compressor, respectively; and η is the efficiency, the subscripts HSA, REC, INV, and m refer to the HSA, the rectifier, the inverter, and the mechanical efficiency, respectively.

A.4. System Integration. The integration of each submodel is conducted via an interconnecting plena approach, as shown below

$$\frac{\mathrm{d}P}{\mathrm{d}t} = \frac{R_{\mathrm{g}}T}{V}(\dot{m}_{\mathrm{in}} - \dot{m}_{\mathrm{out}}) \quad (67)$$

where T, P, and V are the temperature, pressure, and volume of the component, respectively; and R_{g} is the gas constant.

AUTHOR INFORMATION

Corresponding Author

Dong Ni − *College of Control Science and Engineering, Zhejiang University, Hangzhou 310027, China;* orcid.org/0000-0002-2227-2555; Email: dni@zju.edu.cn

https://doi.org/10.1021/acs.iecr.2c01784
Ind. Eng. Chem. Res. 2022, 61, 13532−13558

Authors

Gang Xiao − *State Key Laboratory of Clean Energy Utilization, Zhejiang University, Hangzhou 310027, China*; orcid.org/0000-0001-6761-8380

Jiamin Yang − *State Key Laboratory of Clean Energy Utilization, Zhejiang University, Hangzhou 310027, China*

Complete contact information is available at: https://pubs.acs.org/10.1021/acs.iecr.2c01784

Notes

The authors declare no competing financial interest.

■ ACKNOWLEDGMENTS

The authors gratefully acknowledge the financial support from (1) the Zhejiang Provincial Natural Science Foundation (no. LR20E060001), (2) the National Natural Science Foundation of China (no. 51776186), and (3) the National Key Research and Development Program of China Grant (no. 2021YFF0500403).

■ NOMENCLATURE

Abbreviations

CSIRO Commonwealth Scientific and Industrial Research Organization
CSP concentrated solar power
GPC generalize predictive control
HSA high-speed alternator
MGT micro gas turbine
MHI Mitsubishi Heavy Industries
MIMO multiple-input−multiple-output
MMPC multimodel predictive control
MPC model predictive control
NMPC nonlinear model predictive control
OMSoP optimized microturbine solar power system project
PID proportional−integration−differentiation
RNN recurrent neural network
SOLGATE solar hybrid gas turbine electric power system
SolGATS concentrated solar power micro gas turbine with TES
SOLHYCO solar-hybrid power and cogeneration plants
SOLUGAS solar up-scale gas turbine system
SQP sequential quadratic programming
TCES thermochemical energy storage
TES thermal energy storage

Greek Symbols

α conversion rate
β reciprocal of ambient temperature
γ specific heat ratio
ε emissivity
ζ local loss coefficient
η efficiency
λ frictional loss coefficient
π circular constant
ρ density
υ kinematic viscosity
ϕ decline angle of receiver
ω rotational speed

Roman Symbols

ΔH_r standard molar reaction enthalpy
$\boldsymbol{\Delta u}$ input's increment
A coefficient matrix
A area
AR ratio of aperture diameter over cavity inner diameter
$\mathbf{B}$ coefficient matrix
$\mathbf{C}$ coefficient matrix
C_p specific heat of constant pressure
C_t amount of substance of reactant
C_v specific heat of constant volume
d disturbance
D diameter
DNI direct normal irradiance
e thickness
E mathematical expectations
$\boldsymbol{e}$ error, deviation
ER expansion ratio
f Darcy resistance coefficient, Fanning coefficient
g gravitational acceleration
Gr Grashof number
h enthalpy, pressure loss
$\boldsymbol{h}$ correction coefficient
i number of the element
J rotational mechanical inertia
k moment of time, thermal conductivity
L length
M control horizon, total mass, total number of elements
$\dot{m}$ mass flow rate
N turbine rotational speed
Nu Nusselt number
OS overshoot
P prediction horizon, pressure
Pr Prandtl number
PR pressure ratio
PW power, work
$\mathbf{Q}$ penalty coefficient matrix
$\dot{Q}$ energy flux
q penalty coefficient
R thermal resistance
$\mathbf{R}$ penalty coefficient matrix
r penalty coefficient
Ra Rayleigh number
Re Reynolds number
R_g gas constant
$RMSE$ root-mean-square error
R_t reaction rate
$\dot{S}_h$ chemical reaction heat
T temperature
t time
TOT turbine outlet temperature
$\boldsymbol{u}$ input
U heat-transfer coefficient
u_m flow velocity
V velocity, volume
VO valve opening
w weight
x division direction of finite element method
$\boldsymbol{x}$ state
$\boldsymbol{y}$ output
$\hat{\boldsymbol{y}}$ predicted model output

Subscripts

01 compressor inlet
02 compressor outlet
05 turbine inlet
06 turbine outlet
ac convective loss through aperture

https://doi.org/10.1021/acs.iecr.2c01784
Ind. Eng. Chem. Res. 2022, 61, 13532−13558

air	air
amb	ambient
ar	radiative loss through aperture
ave	average
c	control, compressor, cold side
conv	convective heat transfer
cor	corrected
d	about the model disturbance
dm	demand
ecav	outer wall of the receiver
eetube	outer diameter of the outer tubes
eisol	outer diameter of the insulation layer
eitube	outer diameter of the inner tubes
etube	outer tubes
extr	radial external heat transfer
f	frictional loss
field	heliostat field
g	fluid field
gt	gas turbine
h	hot side, hydraulic diameter
HSA	high-speed alternator
i	number of the element
icav	inner side of cavity
ietube	inner diameter of the outer tubes
iitube	inner diameter of the inner tubes
in	inlet, incident
INV	inverter
isol	insulation layer
isolb	insulation layer at the bottom
itube	inner tubes
j	local loss
load	power load
loss	thermal loss
M	lumped bulk
max	maximum
min	minimum
mir	heliostat mirror
out	output
oxi	oxidation reaction
p	prediction
r	radial
rcp	recuperator
rcv	receiver
REC	rectifier
red	reduction reaction
s	solid field
set	setpoint
t	turbine
tube	absorption tubes
u	about the model input
use	the heat absorbed by airflow
wicav	inner wall of cavity
z	bottom

REFERENCES

(1) Yee, S.; Milanovic, J.; Hughes, F. Overview and Comparative Analysis of Gas Turbine Models for System Stability Studies. *IEEE Trans. Power Syst.* **2008**, *23*, 108−118.

(2) Quero, M.; Korzynietz, R.; Ebert, M.; Jiménez, A. A.; del Río, A.; Brioso, J. A. Solugas - Operation Experience of the First Solar Hybrid Gas Turbine System at MW Scale. *Energy Proc.* **2014**, *49*, 1820−1830.

(3) Schwarzbözl, P.; Buck, R.; Sugarmen, C.; Ring, A.; Crespo, M. J. M.; Altwegg, P.; et al. Solar gas turbine systems: Design, cost and perspectives. *Solar Energy* **2006**, *80*, 1231−1240.

(4) Wacek, E.; Ferguson, W. *Application of the Latest Aeroderivative Gas Turbine Technology*. 09-IAGT 203; General Electric, 2009.

(5) Spelling, J.; Guédez, R.; Laumert, B. A Thermo-Economic Study of Storage Integration in Hybrid Solar Gas-Turbine Power Plants. *J. Sol. Energy Eng.* **2014**, *137*, 011008.

(6) Yang, J.; Xiao, G.; Ghavami, M.; Al-Zaili, J.; Yang, T.; Sayma, A.; et al. Thermodynamic modelling and real-time control strategies of solar micro gas turbine system with thermochemical energy storage. *J. Clean. Prod.* **2021**, *304*, 127010.

(7) Singh, A.; Tescari, S.; Lantin, G.; Agrafiotis, C.; Roeb, M.; Sattler, C. Solar thermochemical heat storage via the Co_3O_4/CoO looping cycle: Storage reactor modelling and experimental validation. *Solar Energy* **2017**, *144*, 453.

(8) Yang, G.; Xiao, G.; Yang, T.; Ni, M.; Cen, K. *Thermal Kinetics of CuO/Cu2O redox system*; SolarPaces, 2017.

(9) Zhou, X.; Xu, H.; Xiang, D.; Chen, J.; Xiao, G. Design and modeling of a honeycomb ceramic thermal energy storage for a solar thermal air-Brayton cycle system. *Energy* **2022**, *239*, 122405.

(10) European Commission. *SOLGATE-Solar Hybrid Gas Turbine Electric Power System*, 2005.

(11) Sinai, J.; Sugarmen, C.; Fisher, U. Adaptation and Modification of Gas Turbines for Solar Energy Applications. *Turbo ExpoPower for Land, Sea, and Air*; ASME, 2005.

(12) Heller, P.; Pfänder, M.; Denk, T.; Tellez, F.; Valverde, A.; Fernandez, J.; et al. Test and evaluation of a solar powered gas turbine system. *Solar Energy* **2006**, *80*, 1225.

(13) Amsbeck, L.; Buck, R.; Heller, P.; Jedamski, J.; Uhlig, R. Development of a tube receiver for a solar-hybrid microturbine system. *14th Biennial CSP SolarPACES Symposium 2008*, 2008.

(14) Heller, P.; Jedamski, J.; Amsbeck, L.; Uhlig, R.; Ebert, M.; Svensson, M.; et al. *Development of a Solar-Hybrid Microturbine System for a Mini-Tower*; SolarPACES, 2009.

(15) Amsbeck, L.; Denk, T.; Ebert, M.; Gertig, C.; Rehn, J. *Test of a Solar-Hybrid Microturbine System and Evaluation of Storage Deployment*; SolarPACES, 2010.

(16) European Commission. *Solar-hybrid Power and Cogeneration Plants*, 2011.

(17) Korzynietz, R.; Quero, M.; Uhlig, R. *SOLUGAS-future solar hybrid technology*; SolarPACES, 2012.

(18) Korzynietz, R.; Brioso, J. A.; del Río, A.; Quero, M.; Gallas, M.; Uhlig, R.; et al. Solugas-Comprehensive analysis of the solar hybrid Brayton plant. *Solar Energy* **2016**, *135*, 578.

(19) Ssebabi, B.; Dinter, F.; van der Spuy, J.; Schatz, M. Predicting the performance of a micro gas turbine under solar-hybrid operation. *Energy Convers. Manage.* **2019**, *177*, 121−135.

(20) Lanchi, M.; Montecchi, M.; Crescenzi, T.; Mele, D.; Miliozzi, A.; Russo, V.; et al. Investigation into the Coupling of Micro Gas Turbines with CSP Technology: OMSoP Project. *Energy Proc.* **2015**, *69*, 1317−1326.

(21) Ghavami, M.; Alzaili, J.; Sayma, A. I. A Comparative Study of the Control Strategies for Pure Concentrated Solar Power Micro Gas Turbines. *ASME Turbo Expo 2017: Turbomachinery Technical Conference and Exposition*, 2017.

(22) Hiromi, N.; Toshiyuki, O.; Kazuta, K.; Masaharu, W.; Masashi, T. Development of Concentrated Solar Power Generation System with Hot Air Turbine. *Mitsubishi Heavy Industries Technical Review*, 2012; Vol. *49*.

(23) CSIRO. *Solar Air Turbine Project-Final Report: Project Results*, 2014.

(24) Kohlenbach, P. Solar cooling with absorption chillers: control strategies and transient chiller perfomance. Doctor of Engineering, Technical University of Berlin, 2006.

(25) Wolfson, R. L. T.; Harvey, H. S. Experimental Comparison of Control Strategies for Solar Energy Systems Incorporating Dual Storage Tanks. *J. Sol. Energy Eng.* **1981**, *103*, 47−51.

https://doi.org/10.1021/acs.iecr.2c01784
Ind. Eng. Chem. Res. 2022, 61, 13532−13558

(26) Powell, K. M.; Edgar, T. F. Modeling and control of a solar thermal power plant with thermal energy storage. *Chem. Eng. Sci.* **2012**, *71*, 138−145.
(27) Menchinelli, P.; Bemporad, A. Hybrid Model Predictive Control of a Solar Air Conditioning Plant. *Eur. J. Control* **2008**, *14*, 501−515.
(28) Zambrano, D.; Garcia-Gabin, W. Hierarchical Control of a Hybrid Solar Air Conditioning Plant. *Eur. J. Control* **2008**, *14*, 464−483.
(29) Juuso, E. K.; Yebra, L. J. Smart adaptive control of a solar collector field. *IFAC Proc. Vol.* **2014**, *47*, 2564−2569.
(30) Menéndez, R.; Martínez, J.; Prieto, M.; Barcia, L.; Sánchez, J. A Novel Modeling of Molten-Salt Heat Storage Systems in Thermal Solar Power Plants. *Energies* **2014**, *7*, 6721−6740.
(31) Leo, J.; Davelaar, F.; Besançon, G.; Voda, A. Control for hybrid combined cycle withparabolic trough and molten-salt storage. *IFAC-PapersOnLine* **2015**, *48*, 439−444.
(32) Nia, A. Z.; Grebenyuk, V.; Nagamune, R. Modeling and control for an integrated thermal hydronic system. *Electrical & Computer Engineering*, 2015.
(33) Prieto, M. J.; Barcia, L. A.; Martinez, J. A.; Villegas, P. J.; Peon, R. Optimizing the Control Strategy of Molten-Salt Heat Storage Systems in Thermal Solar Power Plants. *Industry Applications Society Meeting 2016*, 2016.
(34) Leo, J.; Davelaar, F.; Besancon, G.; Voda, A. Modeling and control of a two-tank molten salt thermal storage for a concentrated solar plant. *Control Conference 2017*, 2017.
(35) Prieto, M.; Martínez, J. A.; Peón, R.; Barcia, L. A.; Nuño, F. On the Convenience of Using Simulation Models to Optimize the Control Strategy of Molten-Salt Heat Storage Systems in Solar Thermal Power Plants. *Energies* **2017**, *10*, 990.
(36) Navas, S. J.; Rubio, F. R.; Ollero, P.; Lemos, J. M. Optimal Control of Solar Thermal Plants with Energy Storage. *17th European Control Conference (ECC)*, 2018
(37) Li, W.; Xiu, D.; Jia, W. Automatic control strategies for disturbance rejection in a solar fresh air system coupled with latent heat thermal storage tank. *Control & Decision Conference 2016*, 2016.
(38) López-Alvarez, M.; Flores-Tlacuahuac, A.; Sandoval, L. R.; Rivera-Solorio, C. Optimal Start-Up Policies for a Solar Thermal Power Plant. *Ind. Eng. Chem. Res.* **2017**, *57*, 1026.
(39) Patrón, G. D.; Ricardez-Sandoval, L. An integrated real-time optimization, control, and estimation scheme for post-combustion CO_2 capture. *Appl. Energy* **2022**, *308*, 118302.
(40) Traverso, A.; Calzolari, F.; Massardo, A. Transient Analysis of and Control System for Advanced Cycles Based on Micro Gas Turbine Technology. *J. Eng. Gas Turbines Power* **2005**, *127*, 340−347.
(41) van Essen, H. A.; Lange, H. C. D. Nonlinear Model Predictive Control Experiments on a Laboratory Gas Turbine Installation. *J. Eng. Gas Turbines Power* **2001**, *123*, 347−352.
(42) Jurado, F. Hammerstein-model-based predictive control of micro-turbines. *Int. J. Energy Res.* **2006**, *30*, 511−521.
(43) Vroemen, B. G.; Essen, H. A. V.; Steenhoven, A. A. V.; Kok, J. J. Nonlinear Model Predictive Control of a Laboratory Gas Turbine Installation. *ASME 1998 International Gas Turbine and Aeroengine Congress and Exhibition*, 1998.
(44) Essen, H. A. V. Modelling and model based control of turbomachinery. PhD Thesis, Technische Universiteit Eindhoven, 1998.
(45) Diwanji, V.; Godbole, A.; Waghode, N. *Nonlinear Model Predictive Control for Thrust Tracking of a Gas Turbine*; IEEE, 2006.
(46) Jurado, F.; Carpio, J. Improving distribution system stability by predictive control of gas turbines. *Energy Convers. Manag.* **2006**, *47*, 2961−2973.
(47) Wiese, A. P.; Blom, M. J.; Manzie, C.; Brear, M. J.; Kitchener, A. Model reduction and MIMO model predictive control of gas turbine systems. *Control Eng. Pract.* **2015**, *45*, 194−206.
(48) Mu, J.; Rees, D. Approximate model predictive control for gas turbine engines. *Proceedings of the American Control Conference*, 2004.
(49) Mu, J.; Rees, D. Nonlinear Model Predictive Control for Gas Turbine Engines. *American Control Conference 2004*, 2004.
(50) Mu, J.; Rees, D.; Liu, G. P. Advanced controller design for aircraft gas turbine engines. *Control Eng. Pract.* **2005**, *13*, 1001−1015.
(51) Sun, J.; Kolmanovsky, I. V.; Ghaemi, R.; Chen, S. A stable block model predictive control with variable implementation horizon. *Automatica* **2007**, *43*, 1945−1953.
(52) Hou, G.; Gong, L.; Huang, C.; Zhang, J. Fuzzy modeling and fast model predictive control of gas turbine system. *Energy* **2020**, *200*, 117465.
(53) Martucci, A.; Fuller, J.; Dorobantu, E.; Rahnamai, K. The Effect of Terminal Weight on the Prediction Horizon of a Gas Turbine Engine Using Model Predictive Control. *ASME Turbo Expo: Power for Land, Sea, and Air 2004*, 2004.
(54) Ghorbani, H.; Ghaffari, A.; Rahnama, M. Constrained model predictive control implementation for a heavy-duty gas turbine power plant. *WSEAS Trans. Syst. Control* **2008**, *3*, 507−516.
(55) Kim, J. S.; Powell, K. M.; Edgar, T. F. Nonlinear model predictive control for a heavy-duty gas turbine power plant. *American Control Conference*, 2013.
(56) SÁez, D.; Milla, F.; Vargas, L. S. Fuzzy Predictive Supervisory Control Based on Genetic Algorithms for Gas Turbines of Combined Cycle Power Plants. *IEEE Trans. Energy Convers.* **2007**, *22*, 689−696.
(57) Mohamed, O.; Wang, J.; Khalil, A.; Limhabrash, M. Predictive control strategy of a gas turbine for improvement of combined cycle power plant dynamic performance and efficiency. *SpringerPlus* **2016**, *5*, 980.
(58) Lopez-Montero, E. B.; Wan, J.; Marjanovic, O. Trajectory tracking of batch product quality using intermittent measurements and moving window estimation. *J. Process Control* **2015**, *25*, 115−128.
(59) Aufderheide, B.; Bequette, B. W. Extension of dynamic matrix control to multiple models. *Comput. Chem. Eng.* **2003**, *27*, 1079−1096.
(60) Jeong, D. H.; Lee, J. M. Ensemble learning based latent variable model predictive control for batch trajectory tracking under concept drift. *Comput. Chem. Eng.* **2020**, *139*, 106875.
(61) Venkat, A. N.; Vijaysai, P.; Gudi, R. D. Identification of complex nonlinear processes based on fuzzy decomposition of the steady state space. *J. Process Control* **2003**, *13*, 473−488.
(62) Schott, K. D.; Bequette, B. W. Control of Chemical Reactors Using Multiple-Model Adaptive Control (MMAC). *IFAC Dynamics and Control of Chemical Reactors (DYCORD +95)*; Elsevier: Copenhagen, Denmark, 1995; pp 345−350.
(63) Zeng, D.; Shan, G.; Diao, S.; Wen, C. A predictive control algorithm based on integrated weighted output of multi-model for boiler turbine system. *IEEE 9th Conference on Industrial Electronics and Applications (ICIEA)*, 2014; pp 629−633.
(64) Li, N.; Li, S.-Y.; Xi, Y.-G. Multi-model predictive control based on the Takagi-Sugeno fuzzy models: a case study. *Inf. Sci.* **2004**, *165*, 247−263.
(65) Xie, S.; Zhou, L.; Ma, A.; Zhou, L. A New Switching Scheme for Multi-model Predictive Control Using Clustering Modeling. *International Conference on Fuzzy Systems & Knowledge Discovery 2008*, 2008.
(66) Kordon, A.; Dhurjati, P. S.; Fuentes, Y. O.; Ogunnaike, B. A. An intelligent parallel control system structure for plants with multiple operating regimes. *J. Process Control* **1999**, *9*, 453.
(67) Wu, Z.; Tran, A.; Ren, Y. M.; Barnes, C. S.; Chen, S.; Christofides, P. D. Model predictive control of phthalic anhydride synthesis in a fixed-bed catalytic reactor via machine learning modeling. *Chem. Eng. Res. Des.* **2019**, *145*, 173.
(68) Wu, Z.; Tran, A.; Rincon, D.; Christofides, P. D. Machine learning-based predictive control of nonlinear processes. Part I: Theory. *AIChE J.* **2019**, *65*, No. e16729.
(69) Wu, Z.; Tran, A.; Rincon, D.; Christofides, P. D. Machine learning-based predictive control of nonlinear processes. Part II: Computational implementation. *AIChE J.* **2019**, *65*, No. e16734.

(70) Ricardez Sandoval, L.; Budman, H. M.; Douglas, P. L. Simultaneous design and control of processes under uncertainty: A robust modelling approach. *J. Process Control* **2008**, *18*, 735−752.
(71) Ricardez-Sandoval, L. A.; Budman, H. M.; Douglas, P. L. Application of Robust Control Tools to the Simultaneous Design and Control of Dynamic Systems. *Ind. Eng. Chem. Res.* **2009**, *48*, 801−813.
(72) Heidarinejad, M.; Liu, J.; Christofides, P. D. Algorithms for improved fixed-time performance of Lyapunov-based economic model predictive control of nonlinear systems. *J. Process Control* **2013**, *23*, 404−414.
(73) Ellis, M.; Durand, H.; Christofides, P. D. A tutorial review of economic model predictive control methods. *J. Process Control* **2014**, *24*, 1156−1178.

https://doi.org/10.1021/acs.iecr.2c01784
Ind. Eng. Chem. Res. 2022, 61, 13532−13558